Spring 5-18-2018

Modeling of Swimming Cells from Nano-Scale to Micro-Scale

Yicheng Zhao
Washinton University in St. Louis

WASHINGTON UNIVERSITY IN ST. LOUIS
School of Engineering and Applied Science
Department of Mechanical Engineering and Materials Science

Thesis Examination Committee:
J. Mark Meacham (Chair)
Philip V. Bayly
David A. Peters

Modeling of Swimming Cells from Nano-Scale to Micro-Scale

by

Yicheng Zhao

A thesis presented to
School of Engineering and Applied Science
of Washington University in St. Louis
in partial fulfillment of the requirements for the degree of
Master of Science

May 2018
St. Louis, Missouri

Contents

List of Figures

List of Tables

Acknowledgments

First and foremost, I would like to thank Dr. Meacham for his guidance throughout this thesis. These works would not be possible without his dedication. I was fortunate to get the opportunity to work with Dr. Bayly. He has always been supportive through my master's study. To the members of the Scalable Integrated Micro-Systems lab, Minji Kim, Michael Binkley, Emma Huff and Husain Shekhani, thank you for both conducting experiments that tie the models back to reality and providing insights that help me finish this study. I would like to thank everyone in the Mechanical Engineering department at Washington University in St. Louis for your help throughout both my undergraduate and graduate studies. Finally, I would like to thank my parents for providing me with all the incredible opportunities. I thank them from the bottom of my heart.

Yicheng Zhao

Washington University in St. Louis

May 2018

Abstract

Certain human genetic diseases -- primary ciliary dyskinesia, infertility, and hydrocephalus -- are characterized by changes in beat frequency and waveform of cilia and flagella. *Chlamydomonas reinhardtii*, which is a single-cell green alga about $10\ \mu m$ in diameter that swims with two flagella, serves as an excellent biological model because its flagella share the same structure and genetic background as mammalian cilia and flagella. This study uses the finite element method to investigate the behavior of *C. reinhardtii* swimming from nano-scale to micro-scale. At the device-level, micro-scale modeling indicates that well-designed acoustic microfluidic devices can be used to trap groups of *C. reinhardtii*, and then the apparent spread of a *C. reinhardtii* population can be correlated to swimming capability through knowledge of the acoustic trapping strength. This finite element model is validated against cell-trapping experiments. At the organism-level, a static nano-scale model is used to study the passive structures of flagella, and a dynamic nano-scale model confirms the theory that steady dynein force (active structures), combined with fluid-structure interactions, can induce flagellar oscillation. These two studies will be connected by a particle tracing model that incorporates the dynamic nano-scale model and the micro-scale model to enable further study of both propulsive forces and the acoustic cell-trapping mechanism.

1 Introduction

1.1 Motivation

Flagella and cilia are slender organelles ($8-12\ \mu m$ long and ~$0.1\ \mu m$ in radius) that have the "$9+2$" passive axoneme structure, consisting of 9 outer doublets, 1 central doublets pair, radial spokes and nexin links as shown in Figure 1.1 (b). The radial spokes connect the central doublets with each outer doublet, and the nexin links connect the outer doublets with their closest neighbors. Active structures, which are dynein molecules and can exert forces, are also present between the closest outer doublets [1]. The combination of the active and passive structures induces oscillation behavior in flagella or cilia, and such behavior can generate a propulsive force that can be used to move cells or fluid [2]. Genetic defects can alter the structure of the active and the passive components, and thus change the propulsive force generated by the beat frequency and the waveform of flagella and cilia. Such changes in mammalian flagella and cilia can cause human diseases, including primary ciliary dyskinesia, infertility, and hydrocephalus [3] [4] [5]. Understanding how defects in flagella and cilia change the beat frequency and waveform is essential to understanding the etiology of these diseases.

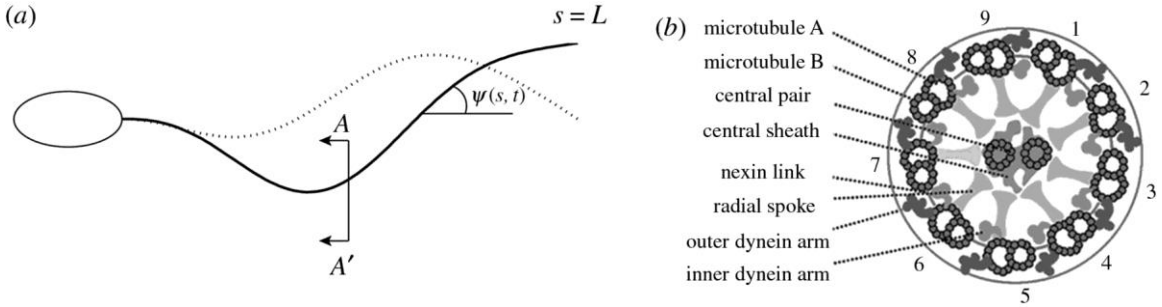

Figure 1.1 (a) Schematic diagram of a *C. reinhardtii* cell with a single flagellum. (b)Schematic diagram of the axial cross section of the flagellum **[2]**.

Human cells with flagella or cilia can be cultured to study the beat frequency and the waveform. However, *C. reinhardtii*, which is a single-cell green alga about $10\ um$ in diameter that swims with two flagella, is used in this study rather than human cells for the following reasons:

- The flagella of *C. reinhardtii* share the same structure and components with human cilia and human sperm flagella, and thus serve as an accurate biological model [6] [7] [8].
- Human cells take much longer to mature ($\sim 60\ days$) than *C. reinhardtii*.
- In general, a single human cell has many cilia, and thus the imaging process to capture a single cilium is very difficult. However, *C. reinhardtii* only has two flagella, so the imaging process is much simpler.

In general, *C. reinhardtii* serves as an excellent biological model for the study of flagella and cilia.

The beat frequency of *C. reinhardtii's* flagella is approximately $\sim 60\ Hz$, so a high-speed camera is required. Also, although flagella are small ($\sim 0.1\ \mu m$ in radius) compared to the cell body ($\sim 10\ \mu m$), *C. reinhardtii* swims very fast in water ($\sim 100\ \mu m/s$) compared to its size [9] [10] [11]. To capture the waveform of flagella, optical microscopes with high resolution are necessary. However, such microscopes do not provide long-duration video of the cells since they will swim out of the field almost immediately. It is thus essential to constrain the swimming cells (either by removing a flagellum or trapping) to enable further study.

Acoustic microfluidics permits non-contact particle manipulation, which can be used for cell trapping [12]. The manipulation of cells arises from the acoustic radiation force which is generated by the acoustic standing waves [13] [14] [15]. Acoustic standing waves are like other standing waves, which have nodes and antinodes, and swimming cells are trapped in the nodes of the standing wave [12] [16]. The nodal locations can be changed by altering the shape of the channels which contain the fluids [17] [18] [19]. Thus single-cell and multi-cell trapping can be achieved by creative design of the channel geometries [20].

There are also mutual benefits between the study of the acoustic microfluidic device and that of the *C. reinhardtii*. The swimming cells will be trapped in pressure nodes. However, they will try to spread out as much as possible in the pressure nodes. The size of the spread is related to both the magnitude of the pressure field and the swimming force of the cells. A well-characterized acoustic microfluidic device can be used to study the swimming force which is also related to the propulsive force generated by the oscillatory waveform of flagella. A type of *C. reinhardtii* with well-characterized swimming force can be used as a probe to measure the pressure field of an acoustic microfluidic device.

The finite element method, which is a computational simulation tool, is used to study both the trapping phenomenon and the oscillatory waveform. This simulation tool is chosen since it makes the design process of acoustic microfluidic devices less costly by predicting the performance without manufacturing the devices. It is also used to study the waveform since experimental works are limited due to the size of flagella.

1.2 The Scope of this Thesis

This thesis summarizes the research where the finite element method is used as a tool to study *C. reinhardtii*.

In Chapter 2, background theories -- acoustic microfluidics, which is the mechanism used to trap swimming cells; steady dynein force theory, which explains the oscillatory waveform of flagella and cilia – are introduced. The general finite element method is then explained with a focus on the building process of a finite element model rather than the actual solver implementation.

In Chapters 3, 4 and 5 three models are described:

- A micro-scale model of acoustic microfluidic devices that are designed to trap groups of swimming cells. The acoustic microfluidics theory is used to build this model.
- A nano-scale model of a single flagellum with the static solution for structural study and dynamic solution for waveform study. The steady dynein force theory is used to build the computational finite element model.
- A particle tracing model that combines the results from the two previous models based on force balancing of acoustic radiation force, drag force, and propulsive force. The acoustic

radiation force will be calculated based on the pressure field of the first model, and the propulsive force will be calculated based on the waveform analysis of the second model.

The micro-scale model is used to design cell-trapping acoustic microfluidic devices by successfully predicting the resonant frequencies and corresponding pressure fields characteristic of a device architecture.

The dynamic nano-scale model helps prove the theory that the oscillatory waveform of flagella can be induced by a steady dynein force together with structure-fluid interactions. This model will also be used for further waveform analysis of flagella too. The static nano-scale model is used to study the structures of flagella together with mathematical models and experiments.

The third ongoing model will be used to study both acoustic microfluidic devices and *C. reinhardtii* together. A well-characterized acoustic microfluidic device can potentially be used to measure the swimming strength of a given *C. reinhardtii* mutant by comparing the spread of the mutant with that of the wild-type. Any mutant that has well-characterized swimming strength can be used to measure the pressure field of a given acoustic microfluidic device as mentioned in the motivation.

This thesis ends with a summary of the results in Chapter 6. Progress made from previous similar models will be discussed, and future work that can improve the current models will be presented.

2 Background Theory

2.1 Acoustic Microfluidics: Device Operation and Particle Manipulation

An acoustic microfluidic device consists of piezoelectric material, transducing material and a fluid domain (typically a channel etched into the transducing material as shown in Figure 2.1. The purpose of any acoustic microfluidic device is to convert electrical oscillation into acoustic oscillation in fluids, which can then generate acoustic radiation force on particles for various uses.

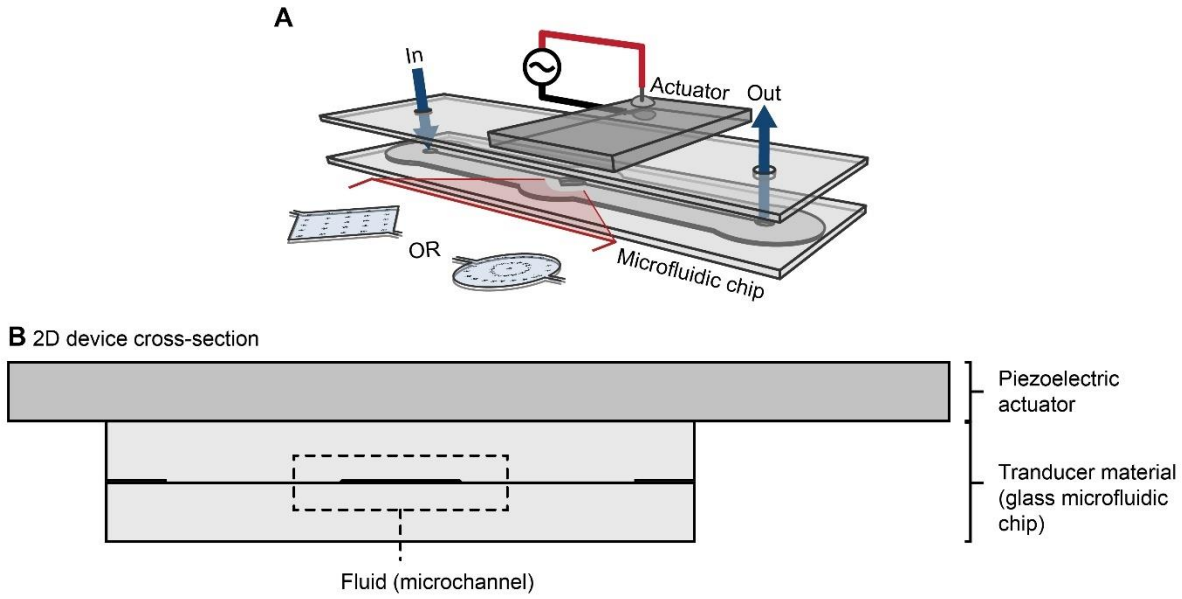

Figure 2.1 Schematic of the experimental setup of the acoustic microfluidic device with square or circle channel etched in the borosilicate: (a) the general view and (b) 2D cross-sectional view.

The electrical oscillation is generated by an alternating current generator and is amplified by a current amplifier. The electrical oscillation is converted into solid vibrations by the piezoelectric material, and then is transduced and possibly magnified by the transducing material. The acoustic oscillation is generated in the fluid at the interface between the fluid and the transducing material. For particle manipulation applications, this acoustic oscillation then induces primary acoustic radiation forces on particles in the fluid due to scattering effects.

2.1.1 Actuating Using a Piezoelectric Material

The relationship between the strain and the stress of solid materials is governed by the constitutive equation. When the strain is small, which is valid for an oscillatory system as the magnitude of oscillation is small, the constitutive equation can be expressed as a linear equation, known as the Hooke's law, as shown below [21]:

$$\boldsymbol{T} = c\boldsymbol{S} \tag{2.1}$$

Where $\boldsymbol{T}$ is the stress tensor and $\boldsymbol{S}$ is the strain tensor. c is the stiffness matrix, which depends on the material properties including Young's Modulus and Poisson's Ratio.

Equation 2.2 can also be expressed as:

$$\boldsymbol{S} = s_E\boldsymbol{T} \tag{2.2}$$

Where s_E is the compliance matrix, which is the inverse of the stiffness matrix ($s_E = c^{-1}$).

However, the constitutive equation for piezoelectric materials is more complicated since not only the stress and the strain are coupled but also the electric field and the current displacement. The equations governing the behavior of piezoelectric material are shown below [22]:

$$\boldsymbol{S} = s_E\boldsymbol{T} + d^T\boldsymbol{E} \tag{2.3}$$

$$\boldsymbol{D} = d\,\boldsymbol{T} + \varepsilon_T\boldsymbol{E} \tag{2.4}$$

Where $\boldsymbol{D}$ is the current displacement, $\boldsymbol{E}$ is the electric field, s_E is the compliance matrix, d is the piezoelectric coupling matrix, d^T is the transverse of the coupling matrix, and ε_T is the electric permittivity. For a given piezoelectric material, 9 parameters need to be known to define all the property matrices including s_E, d, and ε_T.

There are 2 equations and 4 unknown variables including $\boldsymbol{D}$, $\boldsymbol{E}$, $\boldsymbol{S}$, and $\boldsymbol{T}$. This suggests that two more equations are needed.

The force equilibrium equation for solid materials is shown below:

$$0 = \frac{\partial}{\partial i}(T_i) + F_i \tag{2.5}$$

where T_i is the sum of the stresses in i direction and F_i is the body force in i direction ($i = x, y, z$). By neglecting other body forces, F_i only comes from inertial force and can be expressed as:

$$F_i = f(u_i) = -\rho\frac{\partial^2}{\partial t^2}(u_i) \tag{2.6}$$

where ρ is the density of the material and u_i is the displacement of the material in i direction. Also, there is a relationship between the strain and the displacement:

$$\boldsymbol{S} = \boldsymbol{f}(\boldsymbol{u}). \tag{2.7}$$

With ρ known as one of the properties of the material, 3 more equations and 2 more unknown variables (Though $\boldsymbol{F}$ consists of three components in three directions, it is essentially one vector. Similarly, $\boldsymbol{u}$ is also one vector.) are introduced. In total, there are 5 equations and 6 unknown variables, which indicates that 1 more equation is needed.

The charge conservation equation for any given material is shown below:

$$\nabla \cdot \boldsymbol{D} = q \tag{2.8}$$

where $\nabla \cdot \boldsymbol{D}$ is the divergence of the current displacement and q is the charge density, which equals to 0.

Though this equation only has 1 unknown variable, it cannot be solved directly since the boundary conditions are related to both $\boldsymbol{D}$ and $\boldsymbol{E}$.

Now there are 6 equations and 6 unknown variables. The system of equations can be solved with boundary conditions and initial conditions.

Note that all the equations can be formulated into harmonic form by changing all the variables into harmonic form. For example, the displacement field, $\boldsymbol{u} = \boldsymbol{u}(x, y, z, t)$, can be transformed into $\boldsymbol{u} = \boldsymbol{u}(x, y, z)e^{-i\omega t}$, where ω is the oscillation frequency of the system. The harmonic form is used since transient solutions are not necessary. Instead, only $\boldsymbol{u}(x, y, z)$ is of interest for a given frequency, since the system is forced to oscillate by electrical oscillation as stated before. After the reformulation, initial conditions are not needed since the dependent variables are not time-dependent anymore.

The constitutive equations explain how piezoelectric materials convert electrical oscillation into solid vibrations. Changes in the electric field and the current displacement will influence the stress and the strain and thus forced electrical oscillation will induce solid oscillation.

2.1.2 Solid Vibrations in a Transducing Material

Transducing material is used to conduct the solid vibration generated by the piezoelectric material into the fluid channel. The relationship between the stress and the strain of the material is governed by Eq. 2.2. For an isotropic material, only 2 properties are needed to define either the compliance matrix or the stiffness matrix. Once the material property matrix is defined, the governing equation with two unknown variables is ready to be solved with Eq. 2.6, 2.7 and 2.8. The transducing material needs to be coupled with the piezoelectric material through boundary conditions. The coupling condition is that the displacement fields at the contacting surfaces for both the transducing material and the piezoelectric material are the same. In this way, the solid vibration generated by the electrical oscillation in piezoelectric material is conducted into the transducing material. For the research described by this thesis, the transducing material is selected to be borosilicate glass for the following reasons:

- The borosilicate material is easy to etch so that the fluid channel can be readily shaped.
- The borosilicate material is transparent so that the trapping behavior can be observed freely.

Again, as stated in the previous section, the governing equations can be formulated to solve for the harmonic response of the oscillatory system.

2.1.3 Acoustic Pressure Field Generated in a Fluid Channel

The governing equation in harmonic form, which is derived from the Navier-Stokes equation and the conservation of mass equation using the perturbation theory with first-order expansion, for the fluid in the etched channel is [23] [24] [25]:

$$\nabla^2 p_1 = -\left(\frac{\omega}{c}\right)^2 p_1 \tag{2.9}$$

where p_1 is the first order perturbation of the pressure, ω is the angular frequency of the oscillation and c is the speed of sound in the fluid. This equation is essentially in the same form of a general wave equation with c representing the propagation speed of the pressure wave.

The total pressure p can be calculated from the ambient pressure p_0, which is the pressure for the fluid with no perturbation, and the first order perturbation pressure p_1 through the following equation:

$$p = p_o + p_1 \tag{2.10}$$

There are one equation and one unknown, and the equation can be solved with proper boundary conditions.

The coupling between the fluid and the transducing material is necessary for the acoustic oscillation to be induced by the solid vibrations. The coupling is governed by following equations [26]:

$$-\boldsymbol{n}\cdot\left(-\frac{1}{\rho_0}(\boldsymbol{\nabla}p)\right)=-\boldsymbol{n}\cdot(\frac{\partial^2}{\partial^2 t}\boldsymbol{u}) \text{ and} \tag{2.11}$$

$$F_A = p \tag{2.12}$$

where ρ_0 is the density of the fluid and F_A is the force per unit area experienced by the transducing material in the perpendicular direction to the coupling surfaces. The first equation describes the force balance in the fluid between the pressure and the inertial force due to the acceleration forced by the transducing material. The second equation states that the force per unit area experienced by the surface of the transducing materials has the same magnitude as the pressure in the fluid at the boundary surface. These two equations ensure a two-way coupling between the transducing material and the fluid. The oscillatory acceleration in the transducing material generates oscillatory pressure in the fluid, and this pressure exerts forces on the surfaces of the transducing material.

Resonance behavior can be observed for the specific combination of frequency, channel shape, boundary conditions and material properties. When the fluid channel is in resonance, the average magnitude of the pressure within the channel should be a local maximum. The resonance mode is the ideal mode for particle manipulation, since the magnitude of the pressure is relatively large, and the acoustic radiation force is magnified. A resonant pressure field has nodes and anti-nodes. Particles with low compressibility and high density will focus in the pressure node as the pressure variation is the smallest in pressure node.

Now the electrical oscillation is converted into acoustic oscillation through the solid vibrations generated by the piezoelectric material and conducted by the transducing material.

2.1.4 Primary Acoustic Radiation Force Acting on a Suspended Particle

Acoustic radiation force can be exerted on particles in the fluid through the interaction between the particle and the acoustic wave, which is a superposition of the primary acoustic wave and the scattered acoustic wave [14] [27] [28]. When the primary acoustic wave, the original acoustic wave without the presence of particles, encounters a particle in the fluid, it will be partially scattered by the particle due to the compressibility difference. It is through a similar two-way coupling as discussed in the previous section that a primary acoustic radiation force is exerted on particles. The governing equation is derived from the Navier-Stokes equation using the second-order perturbation theory, and is shown below [14]:

$$\boldsymbol{F_{rad}} = -\frac{4\pi}{3}a^3\boldsymbol{\nabla}\left[\frac{1}{2}f_1\kappa_0\langle p_1^2\rangle - \frac{3}{4}f_2\rho_0\langle v_1^2\rangle\right] \tag{2.13}$$

where $\boldsymbol{F_{rad}}$ is the acoustic radiation force, a is the radius of the particle, $f_1$and f_2 are parameters reflecting the influence of differing fluid and particle properties. κ_0 is the compressibility of the fluid, ρ_0 is the density of the fluid, p_1 is the first-order pressure, and v_1 is magnitude of the first-order velocity. $\langle X\rangle$ is the time-averaged X over a full period. The equations for the monopole and dipole coefficients are shown below:

$$f_1 = 1 - \frac{\kappa_p}{\kappa_0} \tag{2.14}$$

$$f_2 = \frac{2(\rho_p - \rho_0)}{2\rho_p - \rho_0} \tag{2.15}$$

where κ_p is the compressibility of the particle and ρ_0 is the density of the particle. For a given system, the properties of the fluid and the particles are known, so the acoustic radiation force can be calculated if p_1 and v_1 are known. The first-order pressure, p_1, can be solved as discussed in the previous section, and the magnitude of the first-order velocity, v_1, can be calculated from p_1.

Now the electric oscillation is converted into the acoustic radiation force exerted on particles in the fluid.

2.2Steady Dynein Force Theory

Many mechanisms are proposed to explain the oscillatory waveform of flagella. Most of them are based on feedback from mechanical deformation to dynein activity [29] [30] [31], which determines the force applied. However, Bayly and colleagues have proposed a steady dynein force theory where the oscillatory waveform is caused by the interaction between steady dynein forces and passive structures [2] [32]. In this theory, the dynein activity is modeled as opposing steady, distributed tangential forces acting on coupled outer doublets. All the passive structures are modeled as slender beams. The governing equations for a beam are [26]:

$$\rho A \frac{\partial^2}{\partial t^2}(u_x) + \frac{\partial}{\partial x}(N) = f_x \tag{2.16}$$

$$\rho A \frac{\partial^2}{\partial t^2}(u_y) + \frac{\partial^2}{\partial x^2}(M_z) = f_y + \frac{\partial}{\partial x}(m_z) + N\frac{\partial^2}{\partial x^2}(u_y) + \frac{\partial}{\partial x}(u_y)\frac{\partial}{\partial x}(N) \tag{2.17}$$

$$\rho A \frac{\partial^2}{\partial t^2}(u_z) + \frac{\partial^2}{\partial x^2}(M_y) = f_z + \frac{\partial}{\partial x}(m_y) + N\frac{\partial^2}{\partial x^2}(u_z) + \frac{\partial}{\partial x}(u_z)\frac{\partial}{\partial x}(N) \tag{2.18}$$

$$\rho(I_{yy} + I_{zz})\frac{\partial^2}{\partial t^2}(\theta_x) + \frac{\partial}{\partial x}(M_x) = m_x \tag{2.19}$$

where x direction is the axial direction. ρ is the density of the beam and A is the cross-sectional area. I_{yy} and I_{zz} are the moments of inertial for an infinitely small section of the beam around the y direction and in the z direction respectively. u_x, u_y and u_z are the displacements in the x, y and z direction respectively; M_x, M_y and M_z are the internal moments; f_x, f_y and f_z are the external distributed forces; m_x, m_y and m_z are the external distributed moments. θ_x is the rotation in the x direction. N is the internal axial load. If all the external loads, the geometries and the material properties are known, there will be 4 equations and 8 unknowns, which are the displacements, the rotation, the internal moments and the internal axial load. 4 more equations are needed to solve for the unknowns.

The constitutive equations are shown below:

$$N = EA\frac{\partial}{\partial x}(u_x) + N_i \tag{2.20}$$

$$M_y = EI_{yy}\frac{\partial^2}{\partial x^2}(u_y) + M_{z_i} \tag{2.21}$$

$$M_z = EI_{zz}\frac{\partial^2}{\partial x^2}(u_z) + M_{y_i} \tag{2.22}$$

$$M_x = GJ\frac{\partial}{\partial x}(\theta_x) + M_{x_i} \tag{2.23}$$

Where E is the Young's Modulus for the beam, G is the shear modulus and J is the torsion constant for the cross-section of the beam. N_i, M_{x_i}, M_{y_i} and M_{z_i} are the initial values for the axial force and the internal moments respectively. These are all either material properties or known values. Thus, 4 more equations are introduced, and the unknown variables can be solved.

Three assumptions used during the derivation are stated below:

- Deformations of a beam are insignificant compared to the geometry: this assumption can be relaxed through co-rotational formulation method so that models with large deformations are valid using the same set of governing equations.
- The equations are only valid for linear-elastic materials.
- Any cross-section of a beam is perpendicular to the axial direction: this assumption is valid for beams with large length-to-radius ratio.

The numbering system for the outer doublets is shown in Figure 2.2. The theory proposes that doublets 1, 5 and 6 are not experiencing any forces, while for other doublets forces are applied to the doublet $\mathrm{N}+1$ by the doublet N since the dynein arm is attached from doublet N to doublet $\mathrm{N}+1$ as shown in Figure 2.2.

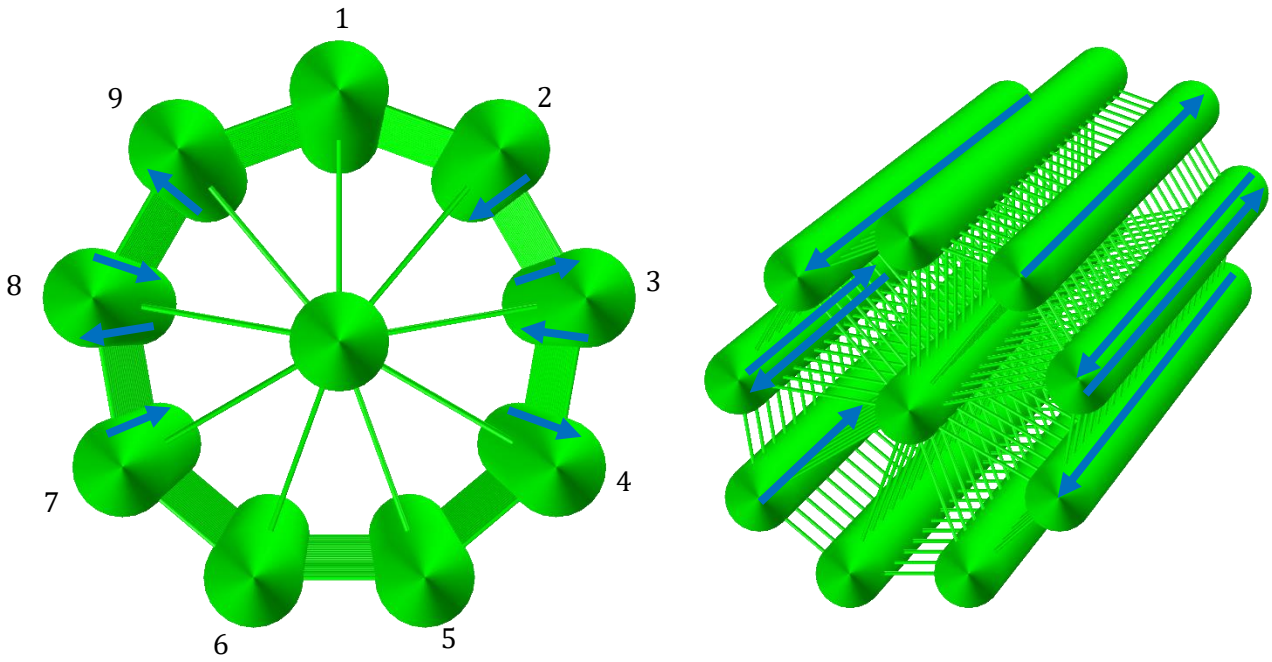

Figure 2.2 Schematic diagram of the numbering system and the dynein forces (blue lines) for the 9-doublet model.

Also, distributed counter moments are added to the doublets arising from the force equilibrium of passive structures [32].

The 6-doublet mode, as shown in Figure 2.3, can be used instead of the 9-doublet model to reduce the computational cost. Doublet 5 and doublet 6 are idle doublets with no forces on them so that they can be combined to 1 doublet. Since the total dynein forces experienced by doublet 3 and doublet 8 are zero, they are removed from the model. This 6-doublet model will be used for the dynamic model since the computational cost for a transient model is high. However, the 9-doublet model will still be used for the static model.

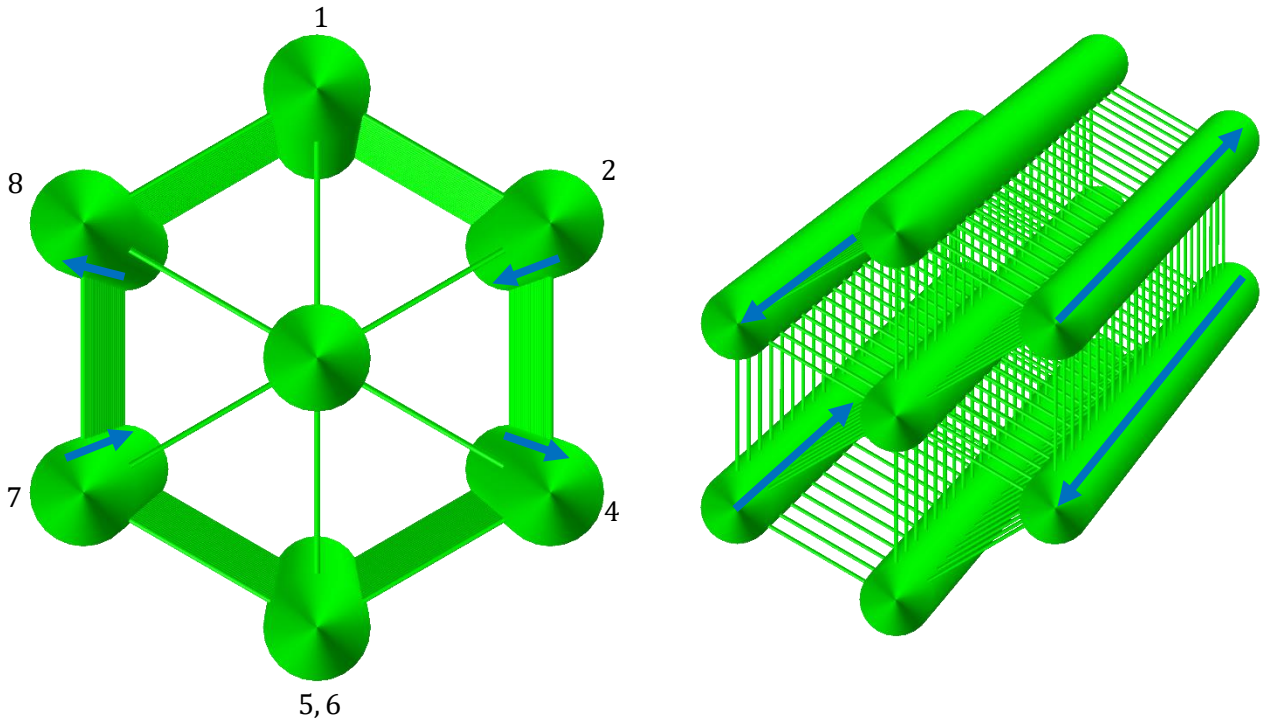

Figure 2.3 Schematic diagram of the numbering system and the dynein forces (blue lines) for the 6-doublet model.

2.3Finite Element Method

The governing equations for all the models are introduced. If all the material properties are known and boundary conditions are set up correctly, the equations can be solved. However, due to the complexity of the equations, it is impossible to generate exact solutions for complicated geometries. Finite element method can be used to approximate the exact solution through discretizing the solution domain into a finite number of elements [33] [34] [35]. This thesis uses COMSOL [26], which is a commercial finite element method software, as the finite element analysis tool to build all the models and solve the governing equations.

The general process of a finite element analysis is shown below:

1. Geometry of the solution domain is set up, so it can be further discretized into a finite number of elements to enable the approximate solution. For instance, a model of an acoustic microfluidic device consists of a piezoelectric material, a transducing material, and an etched fluid channel. All the shapes for the components and the relative positions between them are needed.
2. Physics is chosen for a given geometry. The governing equations are set up to be solved by the finite element method. For example, for a model of an acoustic microfluidic device, governing equations for the piezoelectric material, the transducing material and the fluid channel are needed together with the coupling equations.
3. Material properties and constants are initialized for the governing equations so that the only unknowns are the dependent variables in the equations.
4. Boundary conditions are set, so the dependent variables are ready to be solved.
5. Mesh is set to discretize the solution domain [21] [36] [37].
6. Governing equations are solved on the mesh domain.
7. Quantities of interest are calculated from the solved dependent variables.

In general, the process of the finite element analysis is similar to that of solving differential equations. However, the solution of the finite element analysis is only an approximation of the exact solution since the discretized solution domain is used rather than the continuous solution domain. Degrees of freedom are a measurement of how the solution domain is discretized for a given finite element model. For a finite element model, the solution will be more accurate if it has larger degrees of freedom, which means that the solution domain is discretized into more sub-domain. Theoretically, if a finite element model has infinite degrees of freedom, the approximate solution will

be the same as the exact solution. However, the number of degrees of freedom for a finite element model is the same as the size of the matrix form governing equation. A larger size matrix equation is more computationally expensive. Thus, there is a trade-off between the accuracy of the solution and the computational cost. The number of degrees of freedom increases linearly with that of the mesh elements, and the error between the exact solution and the approximate solution decreases monotonically with the number of degrees of freedom for a properly meshed model. This behavior can be used to check the convergence of the results of a finite element method. At least three models with different numbers of mesh elements need to be solved and a plot of a variable versus the number of degrees of freedom can be generated to check whether the variable converges monotonically with the number of degrees of freedom.

For a model of an acoustic microfluidic device, however, it has already been shown that the model will have good convergence behavior if the maximum size of the mesh elements is 10 times smaller than the wavelength of the acoustic or vibrational wave respectively for the piezoelectric material, the borosilicate, and the fluid.

3 Acoustic Microfluidic Device Model

3.1 Objectives: Investigation of Resonance Frequencies and Pressure Fields

Small particles in the micrometer size range experience acoustic radiation force and migrate to pressure nodes of the acoustic pressure field. In this chapter, a finite element model is built for acoustic microfluidic devices, that are used to trap *C. reinhardtii* based on application of acoustic radiation force theory. Such a model is used to investigate the resonant frequencies and associated pressure fields of a given acoustic microfluidic device, which will then be used to examine the propulsive force of *C. reinhardtii* cells from the computational modeling perspective.

3.2 Procedure

3.2.1 Piezoelectric Material Model: Investigation of Material Properties

The piezoelectric material needs to be modeled correctly to model the entire acoustic microfluidic device accurately. Although nominal properties of the piezoelectric material used in the experiments are provided by the vendor (American Piezo Ceramics, Inc.) [38], actual and reported values can deviate significantly [39]. Such variation in the mechanical and electrical properties will dramatically change the impedance of the piezoelectric material, and thus the stacked impedance of the entire system will also vary. It is essential for the impedance of the model to be as close to that of the experiment.

The dimensions of the piezoelectric materials used in the experiments are $28\ mm \times 24\ mm \times 1.5\ mm$, $28\ mm \times 24\ mm \times 2.0\ mm$ and $28\ mm \times 24\ mm \times 2.5\ mm$ (In $length \times width \times thickness$). Data for the impedance response of these piezoelectric materials with different thicknesses are available from experiments. In the experiments, electrodes are attached to the top and bottom surfaces through the thickness direction.

A 2D model of just the piezoelectric material was used to investigate differences between the impedance response predicted by the model and that measured from experiments. A 2D model is appropriate for the following reasons:

- Piezoelectric materials exhibit transverse material properties when polarized by electrodes [22], and those used for the experiments are polarized in the thickness direction by the applied electrodes. Since the other two dimensions are much greater than the thickness and have the same material properties, the use of a 3D model is not necessary.
- The wavelengths of the fluid calculated from the frequencies of interest are at the same order of the thickness, so the impedance response is mainly influenced by the thickness rather than the length and the width. If the thickness is depicted in the model, the desired impedance response should be captured.
- Compared to a 3D model, the computational cost of a 2D model is much less because a 2D model has significantly fewer degrees of freedom. A 2D model is more accurate than a 1D model since the 2D model captures the spatial effects of the other dimensions as well, while the 1D model does not.

Only one finite element model of the piezoelectric material with the dimension of $28\ mm \times 24\ mm \times 1.5\ mm$ is shown in this paper, but the results for the others can be obtained by changing the piezoelectric thickness in the model.

The geometry of the model is essentially a rectangle with dimensions of $12\ mm \times 1.5\ mm$ representing only half of the piezoelectric material. The model only represents the $width \times thickness$ cross-section of the material, ignoring the effects in the length direction. Only half of the cross-section is modeled since $12\ mm$ is used for width rather than $24\ mm$ by taking advantage of symmetry in the width direction.

Two sets of boundary conditions are established for the Solid Mechanics and the Electrostatics respectively, and the coupling between the two physics are set up using the Piezoelectric Effect.

For the Solid Mechanics Physics, the Free boundary condition is used for all edges except for the one shown in

Figure 3.1 (a). This boundary condition represents a free surface that is not restrained.

The Symmetry boundary condition is used for the symmetry plane represented by the edge as shown in

Figure 3.1 (a). For this edge, $\vec{n} \cdot \vec{u} = 0$, where $\vec{n}$ is the normal vector at the edge and $\vec{u}$ is the displacement vector at the edge [26]. This boundary condition ensures that the magnitude of the displacements perpendicular to the edge is zero.

For the Electrostatics, the Zero Charge boundary condition is set for the two edges as shown in Figure 3.1 (b), because the boundary conditions for a free surface and a symmetry plane are the same for Electrostatics. $\vec{n} \cdot \vec{D} = 0$, where $\vec{n}$ is the normal vector at the edge and $\vec{D}$ is the electric displacement vector at the edge. For a free surface, there are zero charges $\sigma = \vec{n} \cdot \vec{D} = 0$. For a symmetry plane, $\vec{n} \cdot \vec{D} = 0$ since the electric potential is known to be symmetric with respect to the boundary [26].

The Electrical Potential boundary condition is used for the top edge as shown in Figure 3.1 (c) to simulate a positive electrical potential being applied to the electrode at the top surface of the piezoelectric material. $V = V_o$, where V is the electric potential at the edge and $V_o = 10\ volts$.

The Ground boundary condition is used for the bottom edge as shown in Figure 3.1 (d) to simulate the other electrode which, together with the top electrode, creates a pathway for the current. The reasons that $10\ volts$ is selected for the electric potential difference are listed below:

- Impedance only depends on the shape and the material properties, so the variation of the magnitude of the electric potential does not alter the impedance of the system.
- The model is linear, so any change in the magnitude of the electric potential will only change the results linearly. For example, the magnitude of any result of a model with $20\ volts$ electric potential will be 2 times greater than that with $10\ volts$.

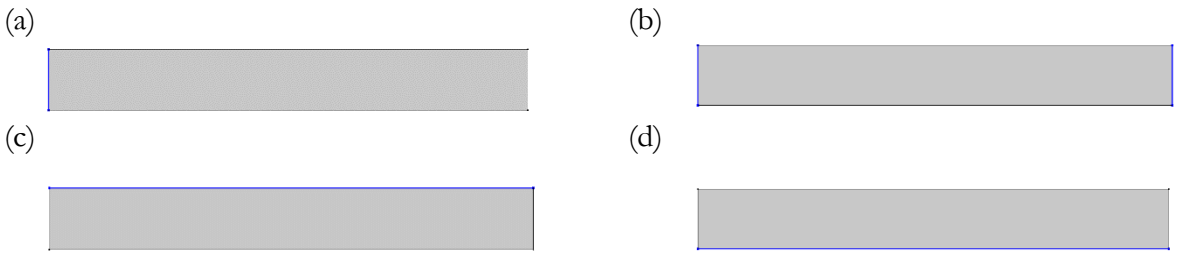

Figure 3.1 Boundary conditions: (a) Symmetry boundary condition, (b) Zero Charge boundary condition, (c) Electric Potential boundary condition and (c) Ground boundary condition.

The mesh is applied as shown in Figure 3.2. The maximum element size is set to be $100\ um$, which is about 10 times smaller than the vibration wavelength of the piezoelectric material driven at the highest frequency. The mesh size that is 10 times smaller than the wavelength yields converged results and no mesh independence study is needed for the model.

A Frequency Domain solver is used for frequencies from $0.3\ MHz$ to $2.5\ MHz$ with a step size of $5 \times 10^{-3} MHz$. Geometric nonlinearity is not included since the vibration displacement is small. Displacement Field and Electric Potential are solved for this model and results are extracted from these two dependent variables.

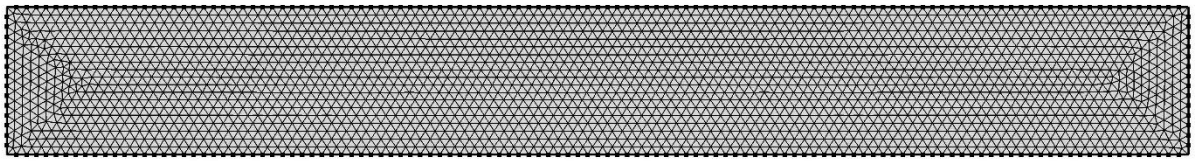

Figure 3.2 The mesh of the piezoelectric material model.

Plots of impedance versus frequency are shown in Figure 3.3, Figure 3.4 and Figure 3.5 for the three thickness values of $1.5\ mm$, $2.0\ mm$ and $2.5\ mm$ respectively, with red lines representing the data from the finite element model and blue lines representing the experimental data. The results are based on material properties summarized in Table 3.1, which give the best fit for experimental data as shown in the plots. In general, the overall impedance predicted from the model is close to the experimental data. Also, the frequencies and magnitudes of the resonance and the anti-resonance predicted by the model are very close to the experimental data; the system is in resonance when the impedance is the lowest, and vice versa for the anti-resonance.

Table 3.1 Properties of the piezoelectric material model that gives the best fit for experimental data.

Properties	Values
Density $\left[{kg}/{m^3}\right]$	7600.00
Stiffness Matrix $[Pa]$	$\begin{bmatrix} 1.60 & 0.95 & 0.92 & 0 & 0 & 0 \\ 0.95 & 1.60 & 0.92 & 0 & 0 & 0 \\ 0.92 & 0.92 & 1.24 & 0 & 0 & 0 \\ 0 & 0 & 0 & 0.27 & 0 & 0 \\ 0 & 0 & 0 & 0 & 0.27 & 0 \\ 0 & 0 & 0 & 0 & 0 & 0.32 \end{bmatrix} \times 10^{11}$
Coupling Matrix $\left[{C}/{m^2}\right]$	$\begin{bmatrix} 0 & 0 & 0 & 0 & 10.60 & 0 \\ 0 & 0 & 0 & 10.60 & 0 & 0 \\ -7.59 & -7.59 & 12.06 & 0 & 0 & 0 \end{bmatrix}$
Relative Permittivity $[1]$	$\begin{bmatrix} 735.00 & 0 & 0 \\ 0 & 735.00 & 0 \\ 0 & 0 & 510.00 \end{bmatrix}$

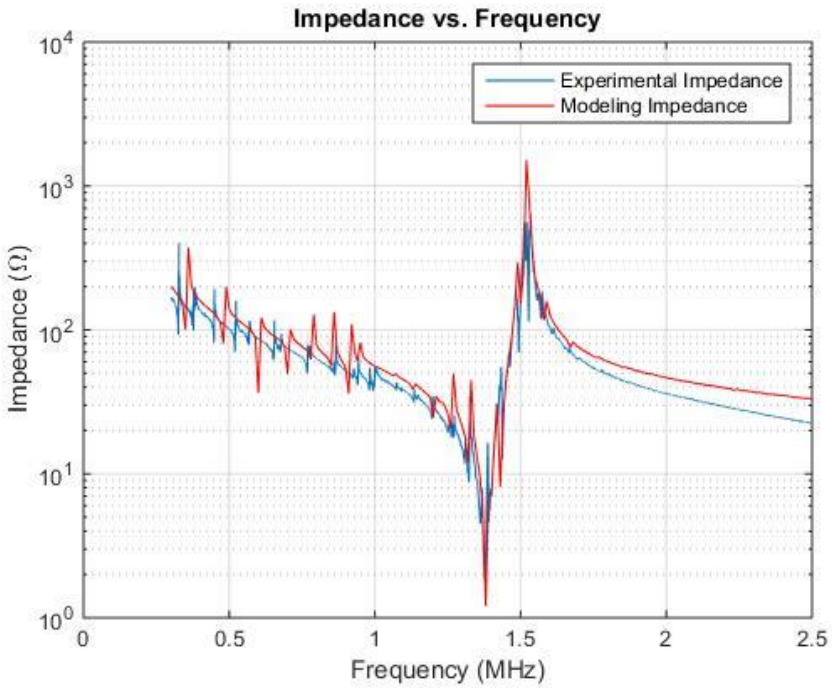

Figure 3.3 Plot of impedance versus frequency for the $\mathbf{1.5}\ \boldsymbol{mm}$ thickness case.

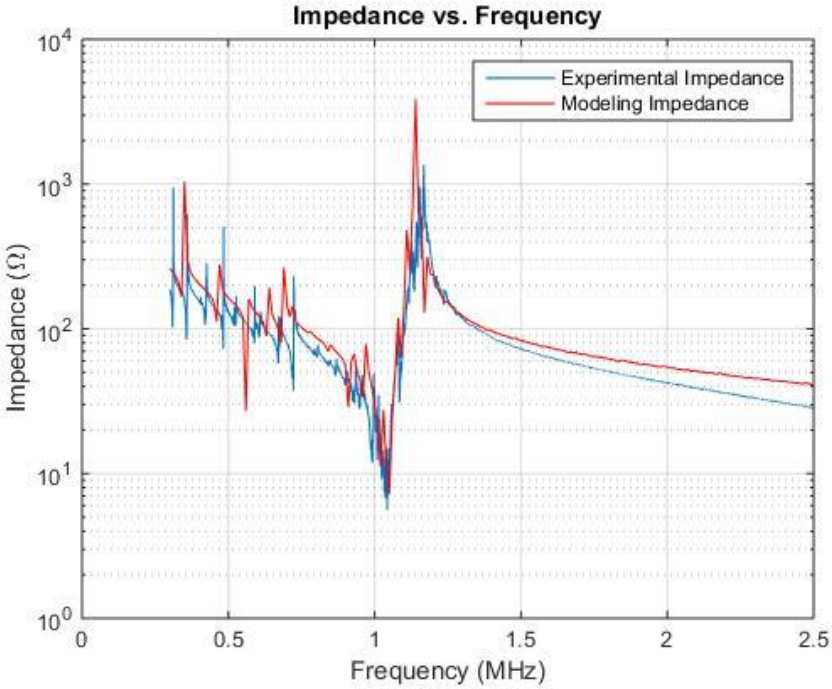

Figure 3.4 Plot of impedance versus frequency for the $\mathbf{2.0}\ \boldsymbol{mm}$ thickness case.

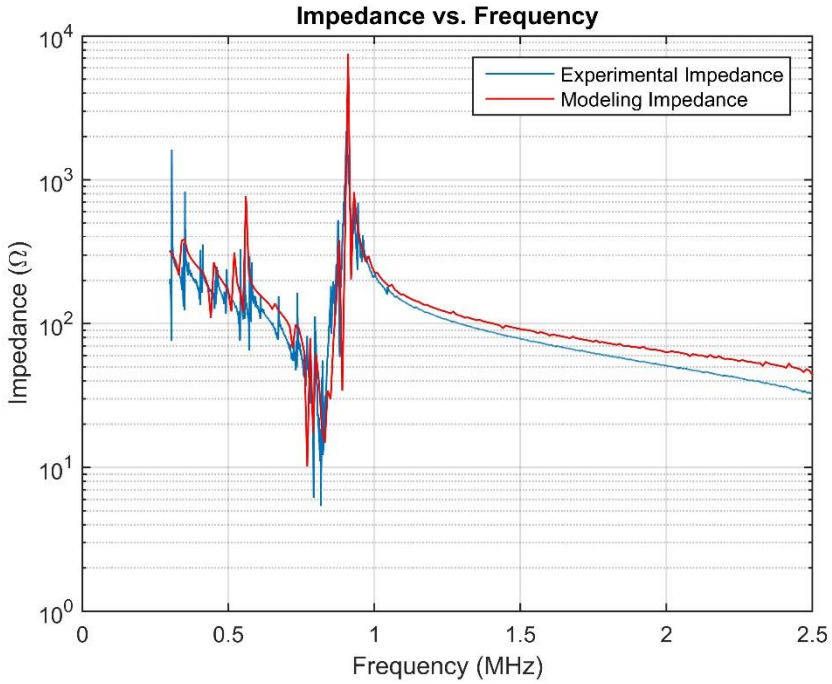

Figure 3.5 Plot of impedance versus frequency for the $\mathbf{2.5}\ \boldsymbol{mm}$ thickness case.

As the results correspond well with the experimental data, the FE model of the piezoelectric material with the given properties is accurate and ready to be used in a more complex model.

3.2.2 2D Acoustic Microfluidic Device Model: Investigation of Resonance Frequencies

Since all the material properties can be selected to accurately represent the the experimental setup, a model of the entire system can be built. A 2D model is built first to identify trends in device behavior before moving to a 3D model. As stated before, a 3D model has many more degrees of freedom than a 2D model, so it is more computationally expensive. Using a 2D model for a wide frequency range helps to determine the resonance frequencies from the frequency response, and then a 3D model can be evaluated over a narrower frequency range around resonant frequencies to determine the detailed pressure field.

The geometry setup is shown in Figure 3.6. This geometry represents the cross-section in the width and thickness plane. The top rectangle is the piezoelectric material and the two bottom rectangles are the borosilicate glass materials, while the small feature at the center represents the etched channel. A zoomed-in view of the channel cross-sectional area is shown in Figure 3.6 (c). The dimensions are listed in Table 3.2. The piezoelectric material is positioned slightly off center to break the symmetry of the system so that non-symmetric modes of solutions are allowed as in the experiment. Otherwise the system could be simplified with a smaller domain and symmetry boundary conditions.

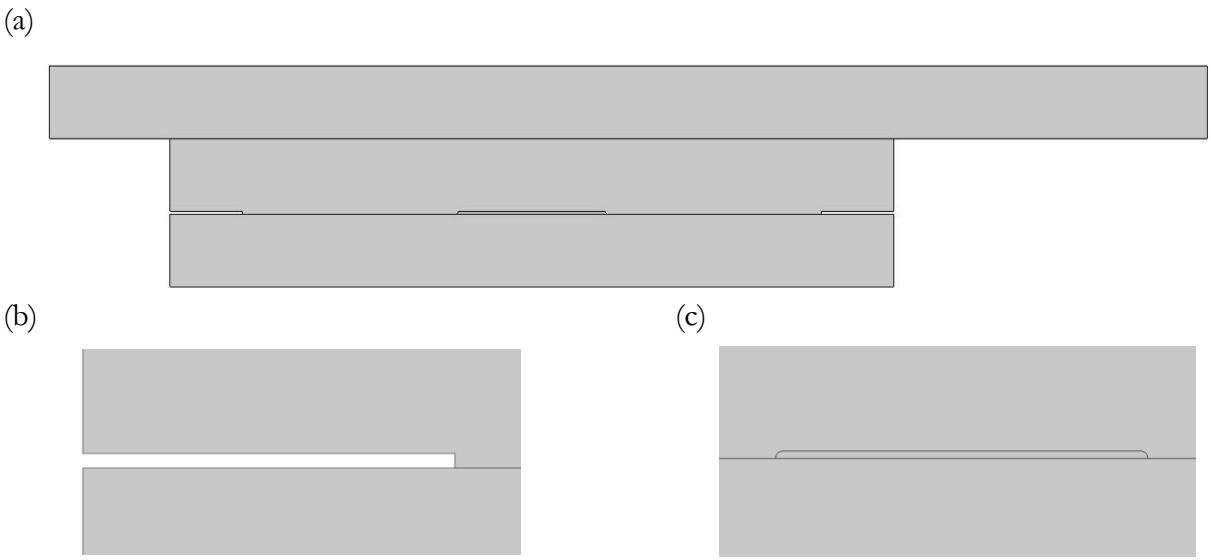

Figure 3.6 Geometry of the 2D model: (a) the general view, (b) the zoomed-in view at the left side of the borosilicate material and (c) the zoomed-in view of the fluid channel at the center.

Table 3.2 The summary of the dimensions for the 2D model.

Dimensions	Values $[\boldsymbol{mm}]$
Glass Thickness	$\mathbf{1.50}$
Glass Width	$\mathbf{15.00}$
Piezoelectric Material Thickness	$\mathbf{1.50}$
Piezoelectric Material Width	$\mathbf{24.00}$
Fluid Channel Thickness	$\mathbf{0.06}$
Fluid Channel Width	$\mathbf{3.09}$
Glass Bounded Width	$\mathbf{12.00}$
Piezoelectric Material Offset	$\mathbf{2.00}$
Fluid Channel Fillet Radius	$\mathbf{0.06}$

There are three different COMSOL physics used in this model: Pressure Acoustics, Solid Mechanics, and Electrostatics. The Pressure Acoustics is used to model the fluid, which is the channel located at the center of the model. The Solid Mechanics is used to model both the glass and the piezoelectric material. The Electrostatics is used to model the piezoelectric material together with the Solid Mechanics. Three sets of boundary conditions are needed since there are three types of physics, including one set of coupling boundary conditions since the interaction between the fluid and the glass needs to be modeled, too. The properties of the materials are summarized in Table 3.3, except for the piezoelectric material properties, which are summarized in Table 3.1.

Table 3.3 The summary of the material properties for the 2D model.

Properties		Values
Fluid (Water)	Density $\left[\boldsymbol{kg/m^3}\right]$	$\mathbf{997.00}$
	Speed of Sound $[\boldsymbol{m/s}]$	$\mathbf{1497.00}$
Glass	Density $\left[\boldsymbol{kg/m^3}\right]$	$\mathbf{2240.00}$
	Young's Modulus $[\boldsymbol{GPa}]$	$\mathbf{60.00}$
	Poisson's Ratio $[\mathbf{1}]$	$\mathbf{0.25}$

For the Electrostatics physics, the same set of boundary conditions is used as in the previous section and is shown in Figure 3.7 (a), (b) and (c). The symmetry boundary condition is not used anymore since the model does not have any symmetry plane.

For the Solid Mechanics physics, the Free boundary conditions are applied to all the outer edges since the vibration is not constrained at any point.

For the Pressure Acoustic physics, coupling boundary conditions, shown in Figure 3.7 (d), are set for all the edges around the shape representing the fluid channel, as discussed in the background theory.

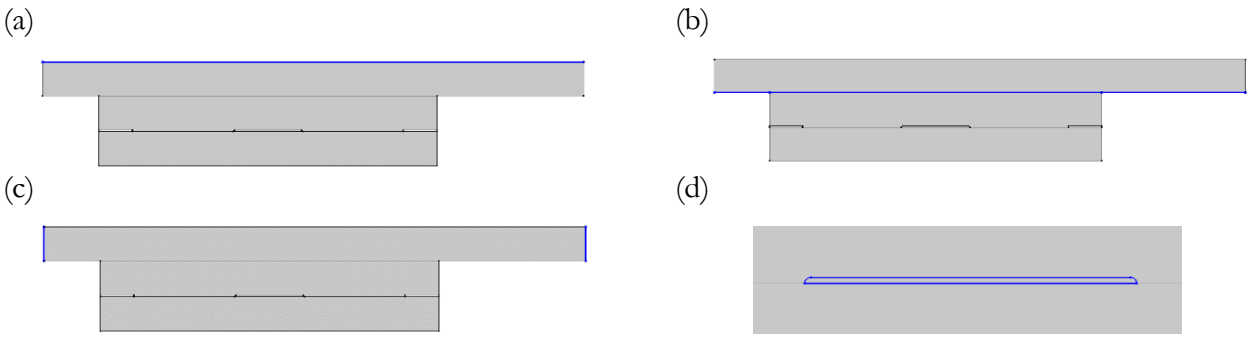

Figure 3.7 Boundary conditions: (a) Electrical Potential, (b) Ground, (c) Zero Charge and (d) Structure-Fluid coupling.

The mesh setup is summarized in Table 3.4. The mesh used for this model is shown in Figure 3.8. Again, the maximum element sizes are set to be about 10 times smaller than the wavelength of the materials to ensure mesh stability. Mesh refinement around the corners is shown in Figure 3.8 (b) and (c).

Table 3.4 Mesh setup for the 2D model.

Materials	Maximum Mesh Sizes $[mm]$	Minimum Mesh Sizes $[mm]$
Piezoelectric Material	0.1	0.006
Glass	0.4	0.006
Fluid Channel	0.01	0.006

(a)

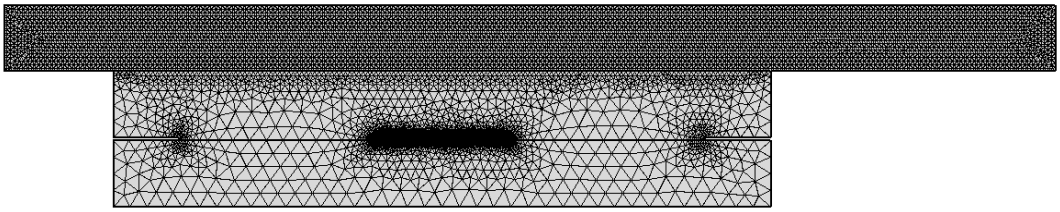

(b) (c)

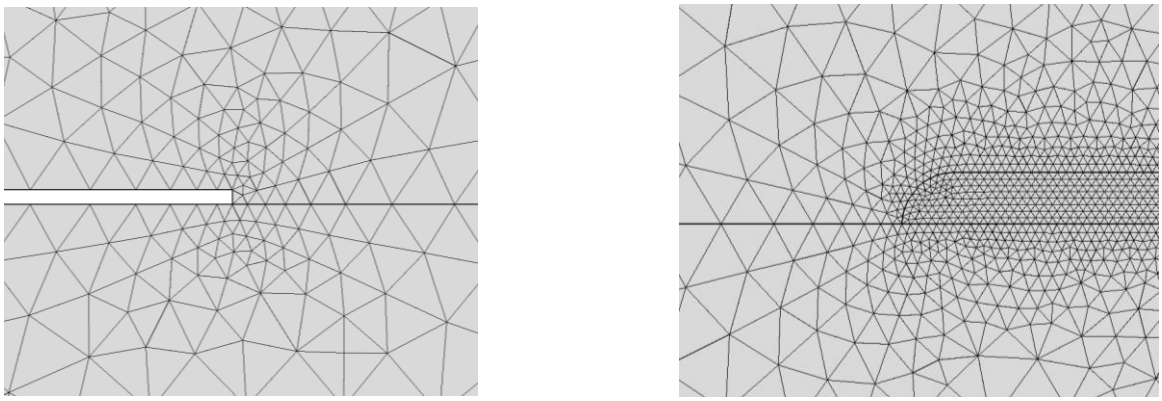

Figure 3.8 The mesh of the 2D model: (a) the general view, (b) the zoomed-in view at the left side of the glass and (c) the zoomed-in view at the fillet of the fluid channel.

A Frequency Domain solver is used for frequencies ranging from $0.5\ MHz$ to $1.3\ MHz$ with a step size of $2 \times 10^{-3} MHz$. Geometric nonlinearity is not included since the vibration displacement is small. Displacement Field, Electric Potential, and Pressure are solved using the model and results are extracted from these three dependent variables.

Absolute pressure is calculated as the magnitude of the pressure since the pressure is complex value due to damping coefficients within the system:

$$p_{absolute} = \sqrt{\left(Im(p)\right)^2 + \left(Re(p)\right)^2}$$

where $Im(p)$ is the imaginary part of the pressure, $Re(p)$ is the real part of the pressure and $p_{absolute}$ is the absolute pressure. For any given frequency, a map of the absolute pressure can be generated within the fluid domain, and an average absolute pressure can be evaluated for the domain. A plot of the average absolute pressure versus frequency can then be generated to find the resonance peak since an average absolute pressure peak indicates a resonance for the fluid channel. The harmonic response of the system is shown in Figure 3.9. Four peaks are identified as they each indicate a lateral resonance of the fluid channel. Other peaks are also considered as resonances. However, through examining the absolute pressure map, most of these modes are found to be due to resonances of the stack of the solid materials.

For the four fluid channel resonances of interest, the absolute pressure maps of the channel are shown beside the peaks. The absolute pressure field is mapped on a white-to-red scale, where a white region indicates a pressure node and a red region indicates a pressure anti-ode. Each absolute pressure map suggests a resonance mode. For example, the third peak shows a 5-node resonance pressure field in 2D. This 2D mode suggests the location of a 5×5-node pressure field in 3D since the other lateral dimension of the chamber has the same width. The frequencies of these peaks will be used to determine the narrower frequency range for the 3D model so that a detailed model around the resonance can be generated and examined.

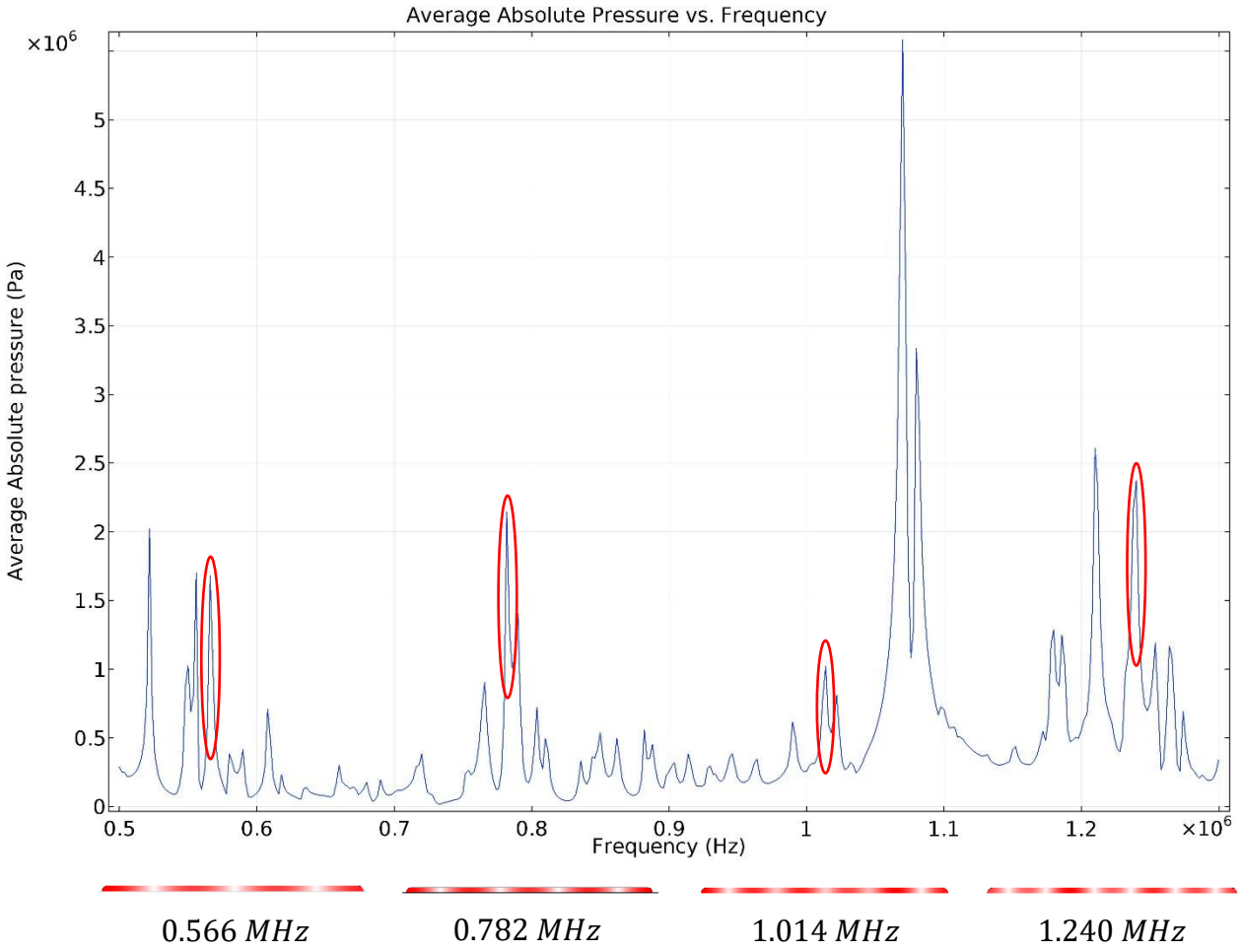

Figure 3.9 Plot of the average absolute pressure in the fluid channel versus frequency. Each resonance mode of the fluid channel is circled in red, and the corresponding mode shape and the frequency are shown below the resonance peak.

3.2.3 3D Acoustic Microfluidic Device Model: Investigation of Pressure Fields

The resonant frequencies found in the previous section can now be used to guide more detailed 3D modeling without needing to perform the analysis over a wide range of frequencies. This allows the 3D model to be as detailed as possible. The 3D model geometry is shown in Figure 3.10, with a top view and a zoomed-in view of the fluid channel. Again, the piezoelectric material is offset to accommodate non-symmetric modes. The dimensions are summarized in Table 3.5.

(a)

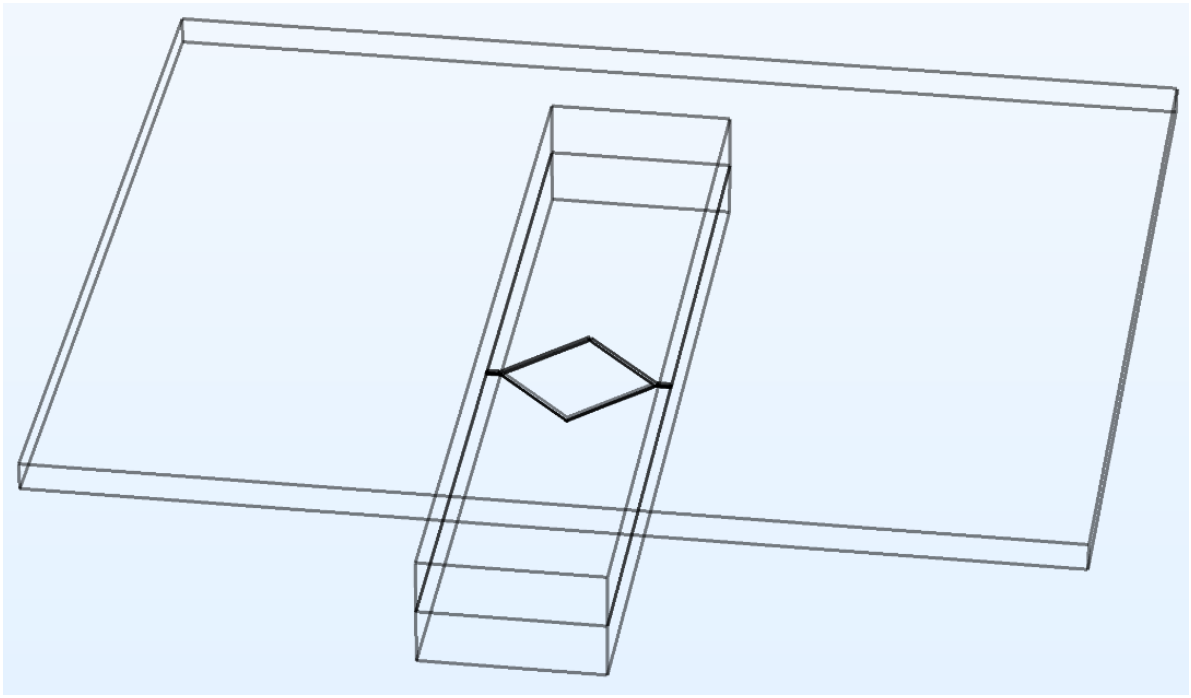

(b)

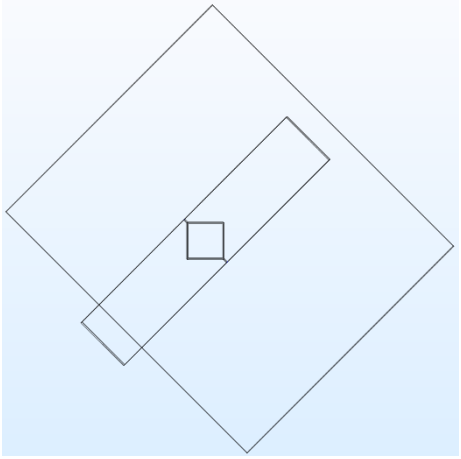

(c)

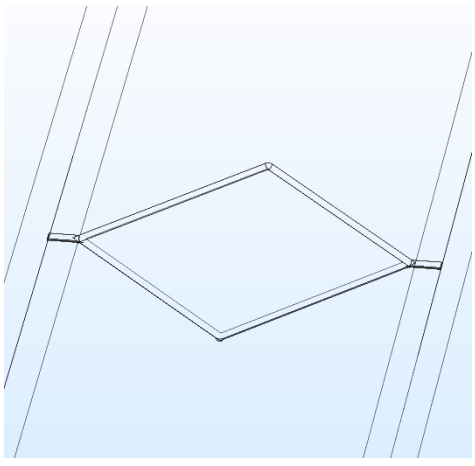

Figure 3.10 Geometry of the 3D model: (a) the general view in 3D, (b) the top view of the whole geometry and (c) the zoomed-in view of the channel.

Table 3.5 The summary of the dimensions for the 3D square channel model.

Dimensions	Values $[\boldsymbol{mm}]$
Piezoelectric Material Thickness	$\mathbf{0.75}$
Piezoelectric Material Width	$\mathbf{24.00}$
Piezoelectric Material Length	$\mathbf{28.00}$
Glass Thickness	$\mathbf{1.50}$
Glass Width	$\mathbf{24.00}$
Glass Length (Not Fully Represented)	$\mathbf{5.00}$
Square Chamber Length and Width	$\mathbf{3.09}$
Square Chamber Thickness	$\mathbf{0.06}$
Inlet and Outlet Channels Width (Length Same as Glass)	$\mathbf{0.14}$
Inlet and Outlet Channels Thickness	$\mathbf{0.06}$
Overall Fillet Radius	$\mathbf{0.06}$

The top box is the piezoelectric material, and the bottom two boxes represent the borosilicate layers with the etched fluid channel in the middle as shown in Figure 3.11. The glass l and the fluid channel are not fully modeled, as those domains are only sections along the channel. These sections contain the essential information about the system, which is the shape of the fluid chamber, as the absolute acoustic pressure within the channel is of interest instead of that within the inlet and outlet. The reasons that the piezoelectric material is represented fully, while the glass and fluid channel are not, are listed below:

- Even a slight increase of the length of the glass and fluid channel in the longitudinal direction increases the model's degrees of freedom by a significant amount since the mesh around the inlet and outlet channels is refined. The length of the piezoelectric material does not affect the degrees of freedom as much since there is no mesh refinement in the piezoelectric domain.

- The length of the piezoelectric material is much smaller than the length of the glass and the fluid channel, so the longitudinal effects cannot be neglected in the piezoelectric domain.

(a)

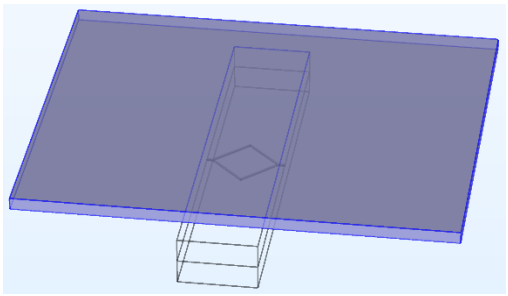

(b)

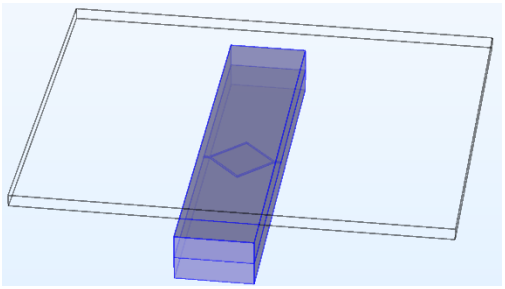

(c)

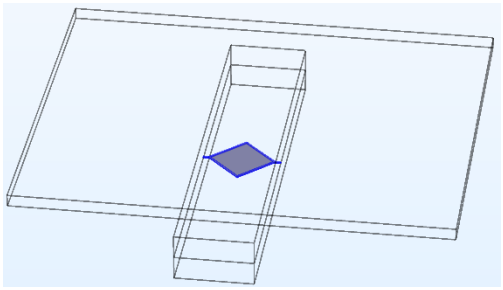

Figure 3.11 Geometry that represents (a) the piezoelectric material, (b) the glass l and (c) the fluid channel respectively.

The types of physics used in this 3D model are the same as those used in the 2D model shown in the previous section; however, boundary conditions are now applied to surfaces instead of edges.

For the Electrostatics, the Electric Potential boundary condition is applied to the top surface of the piezoelectric material as shown in Figure 3.12 (b), and the magnitude is set to be $10\ volts$. Again, since the model is a linear model, any solution can be easily calculated based on the solution from the $10 - volts$ model. The bottom surface of the piezoelectric is set to have a Ground boundary condition as shown in Figure 3.12 (c). Zero Charge boundary conditions are applied to the other surfaces as shown in Figure 3.12 (a).

For the Solid Mechanics, the free boundary condition is applied to all the outer surfaces, except for the cross-sectional surfaces, which are set as Low-Reflecting boundaries as shown in Figure 3.12 (d). The mathematical form is $\boldsymbol{S} \cdot \boldsymbol{n} = -iw\boldsymbol{d_{im}}\boldsymbol{u}$, where $\boldsymbol{S}$ is the stress, $\boldsymbol{n}$ is the normal vector at the surface, $\boldsymbol{d_{im}}$ is the calculated perfect impedance and $\boldsymbol{u}$ is the displacement. This boundary condition determines the perfect impedance for wave propagation with minimum reflection based on the material properties and the frequency, and it simulates the behavior of the wave in linear elastic

materials passing through a surface of which the materials are essentially the same on both sides. This boundary condition models the behavior of an infinitely large domain without introducing too many degrees of freedom.

For the Pressure Acoustics, the Acoustic-Structure boundary conditions are set up for the surfaces, as shown in Figure 3.12 (e)., between the glass and the fluid channel in the same form shown in the previous section for the 2D model. The Plane Wave Radiation boundary condition is set up for the cross-sectional surfaces of the inlet and outlet as shown in Figure 3.12 (f). This boundary condition follows the same logic as the Low-Reflecting boundary condition. It models the behavior of an infinitely large domain without introducing too many degrees of freedom through matching the impedance on both sides of the surface for the pressure wave in the fluid.

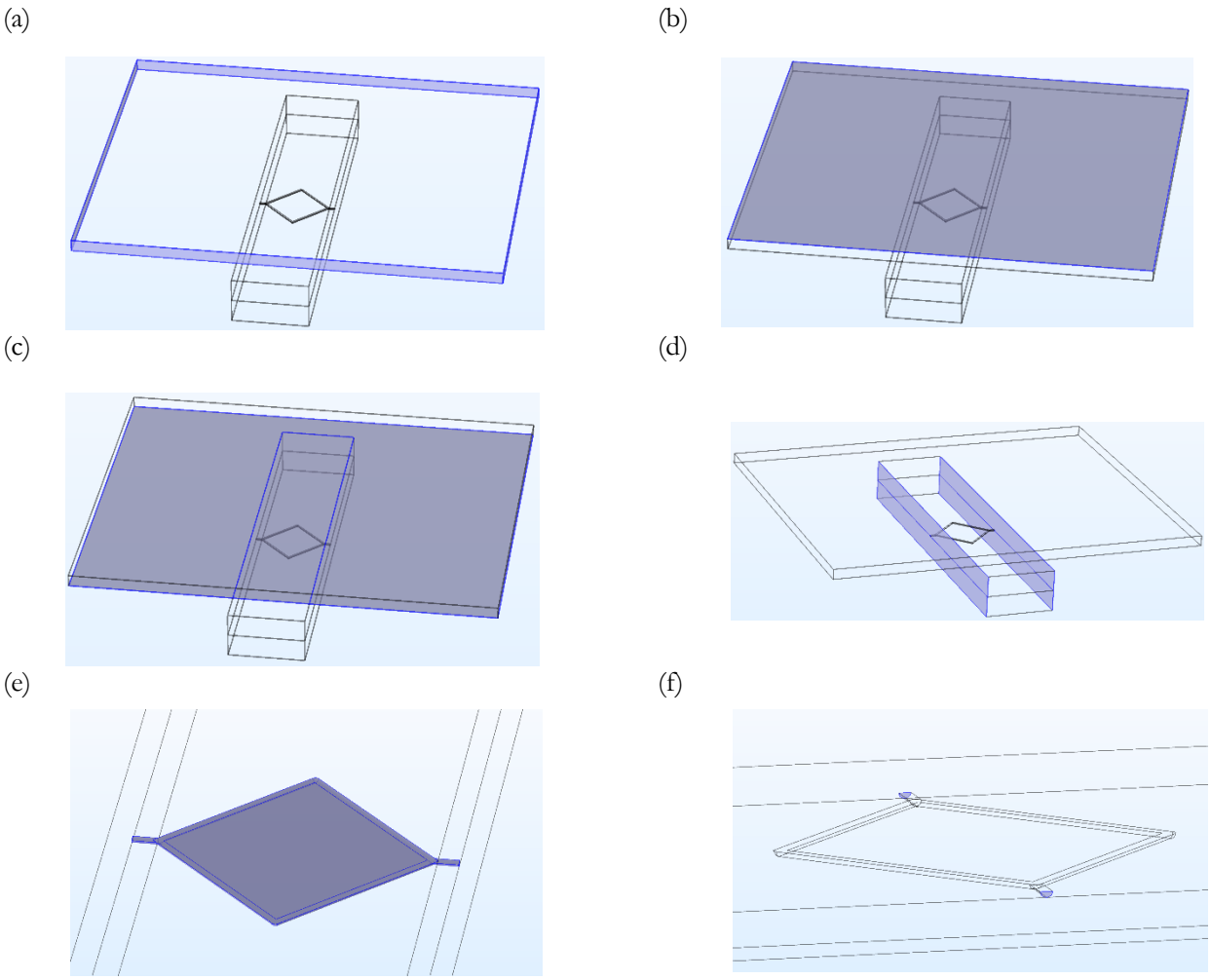

Figure 3.12 Boundary conditions: (a) Zero Charge, (b) Electrical Potential, (c) Ground, (d) Low-Reflecting, (e) Structure-Fluid coupling and (f) Plane-Wave.

The mesh setup is shown in Table 3.6. The mesh used for the model is shown in Figure 3.13 (a)., and a zoomed-in one at the fluid channel with refinement is shown in Figure 3.13 (b).

A Frequency Domain solver is used for frequencies ranging from $0.990\ \text{MHz}$ to $1.100\ \text{MHz}$ with a step of $0.002\ MHz$. Geometric nonlinearity is not included since the vibration displacement is small. Displacement Field, Electric Potential, and Pressure are solved using this model and results are extracted from these three dependent variables.

Table 3.6 Mesh setup for the 3D model

Materials	Maximum Mesh Sizes $[\boldsymbol{mm}]$	Minimum Mesh Sizes $[\boldsymbol{mm}]$
Piezoelectric Material	0.4	0.01
Glass	0.4	0.01
Fluid	0.1	0.01

(a)

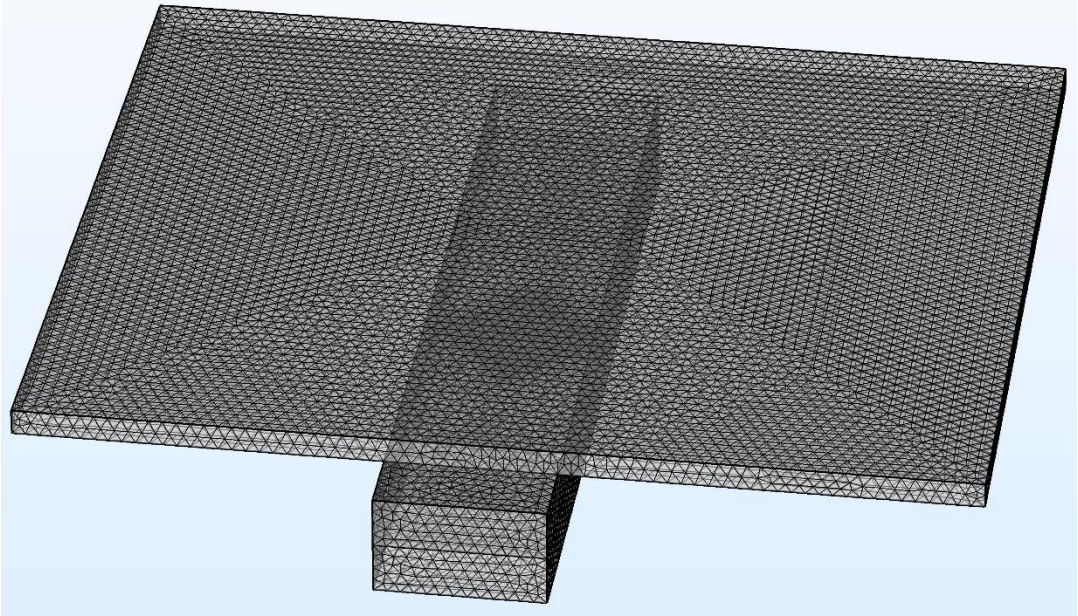

(b)

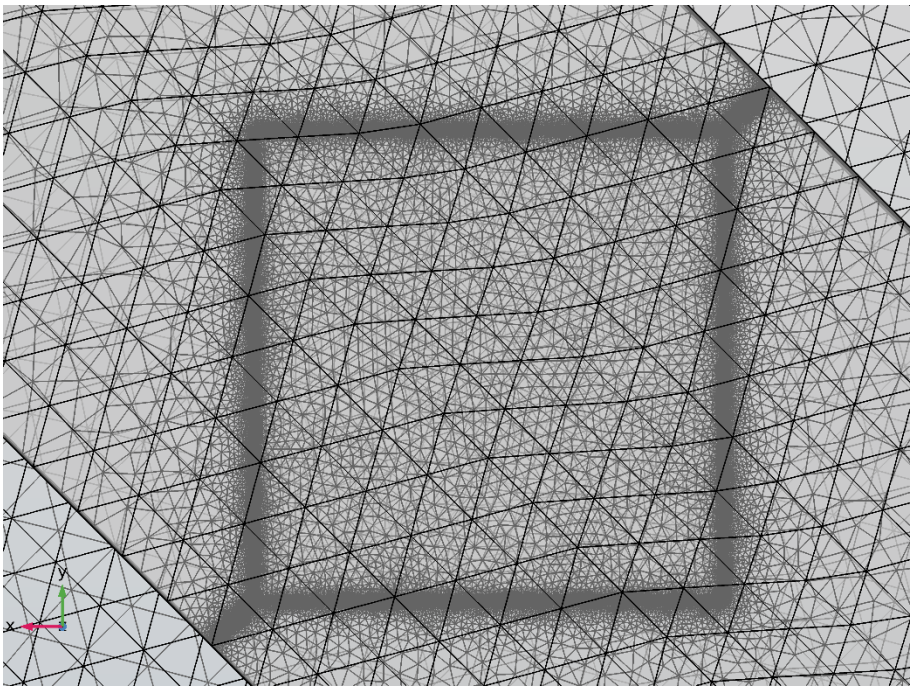

Figure 3.13 Mesh of the 3D model: (a) the general view and (b) the zoomed-in view at the channel.

The model for a circle channel is built using the same procedure except for the geometry of the fluid channel. The geometry is shown in Figure 3.14 (a), and the dimensions are the same as the square channel model except the radius of the circle is $1.55\ mm$. The mesh used is shown in Figure 3.14 (b) and (c).

(a)

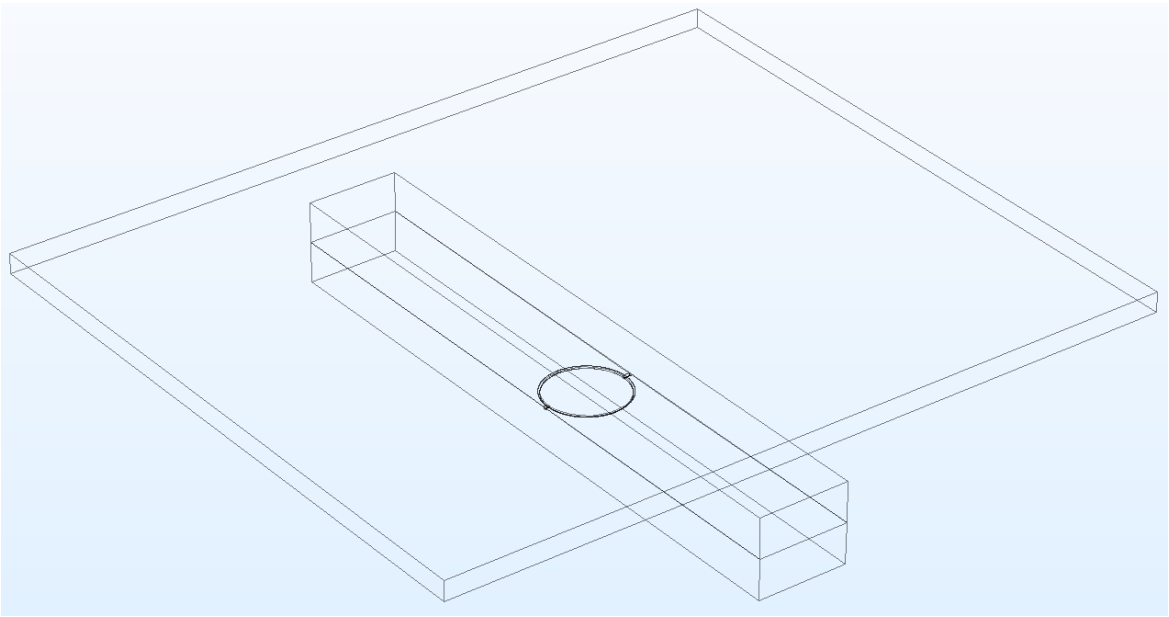

(b) (c)

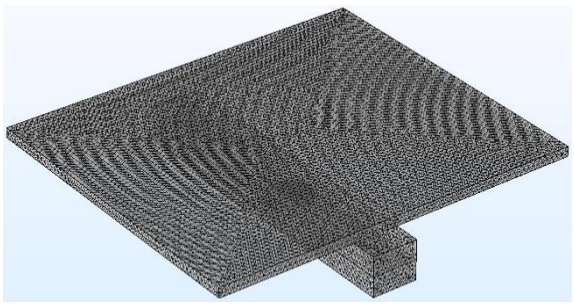

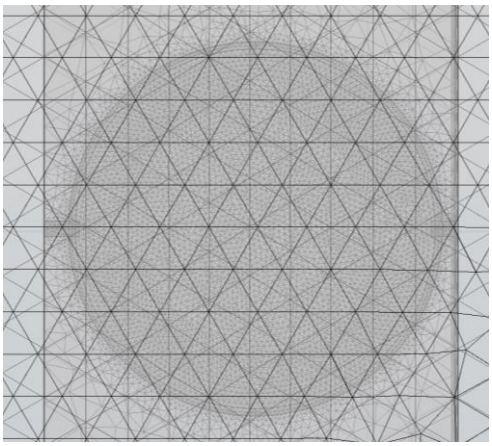

Figure 3.14 (a) Geometry of the 3D model with a circle channel. Mesh of the model: (b) the general view and (b) the zoomed-in view at the circle channel.

A Frequency Domain solver is used for frequencies ranging from $1.050\ \text{MHz}$ to $1.180\ \text{MHz}$ with a step of $0.002\ MHz$.

3.3Results

Results are generated for each of the two models with different chamber shapes. For each shape, the average absolute pressure of the fluid chamber is extracted and plotted versus the frequency, and a contour map of the absolute pressure is generated.

For the square channel, the results are shown in Figure 3.15. The harmonic response plot indicates two resonant frequencies. The absolute pressure field is plotted for the higher peak at ($f = 1.041\ MHz$). The microfluidic device is used to convert the electrical oscillation into acoustic vibration in the chamber. Through the standing pressure field set up by the acoustic vibration, suspended particles will be focused into either pressure node or pressure anti-node. This pressure field exhibits a clear $5x5$ nodal patern suitable for trapping objects, where the white regions represent the trapping locations. Any of the locations can be used to trap groups of swimming *C. reinhardtii*. The result is validated regarding the frequency and mode shape using experimental results as shown in Figure 3.15

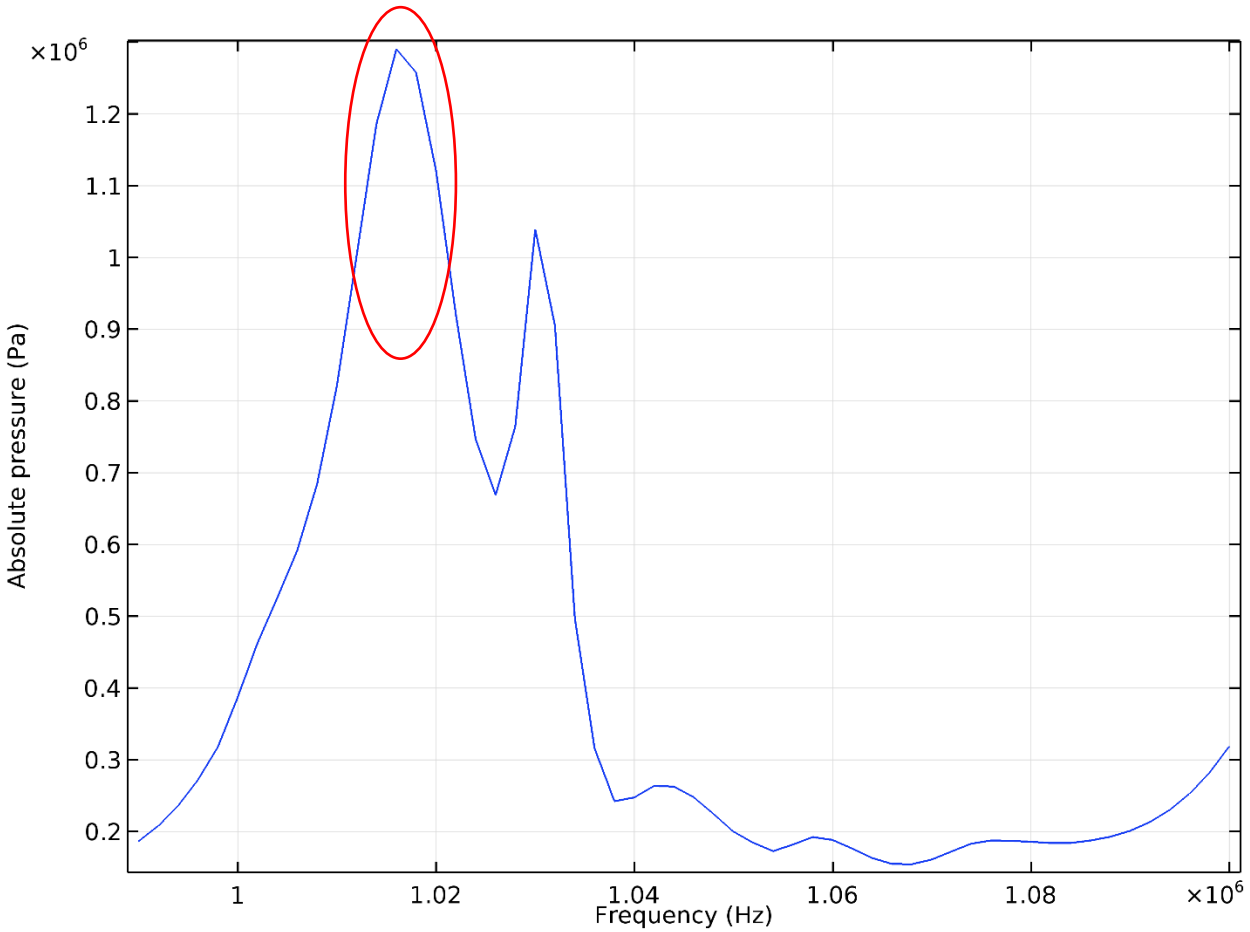

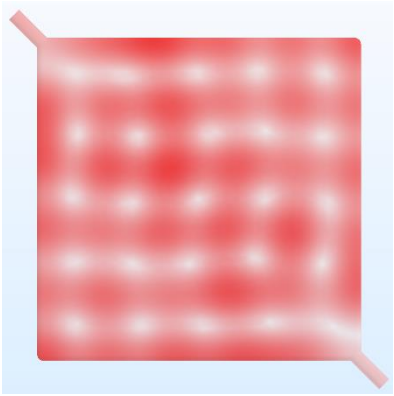

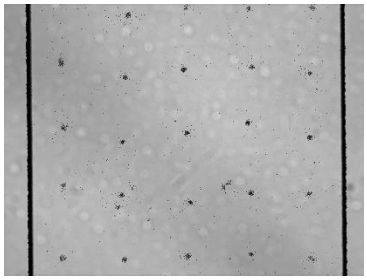

1.014 MHz 1.041 MHz

Figure 3.15 The frequency response of the 3D model for the square channel case is shown at the top. The pressure map at the resonance frequency for the model is shown at the bottom left, compared to the experimental result at the bottom right.

For the circular chamber, the results are shown in Figure 3.16. The frequency response plot indicates one resonant frequency in the range of interest. A map of the absolute pressure field is plotted for this peak at ($f = 1.104\ MHz$). This pressure field shows a central trap that can be used to trap one group of swimming *C. reinhardtii*.

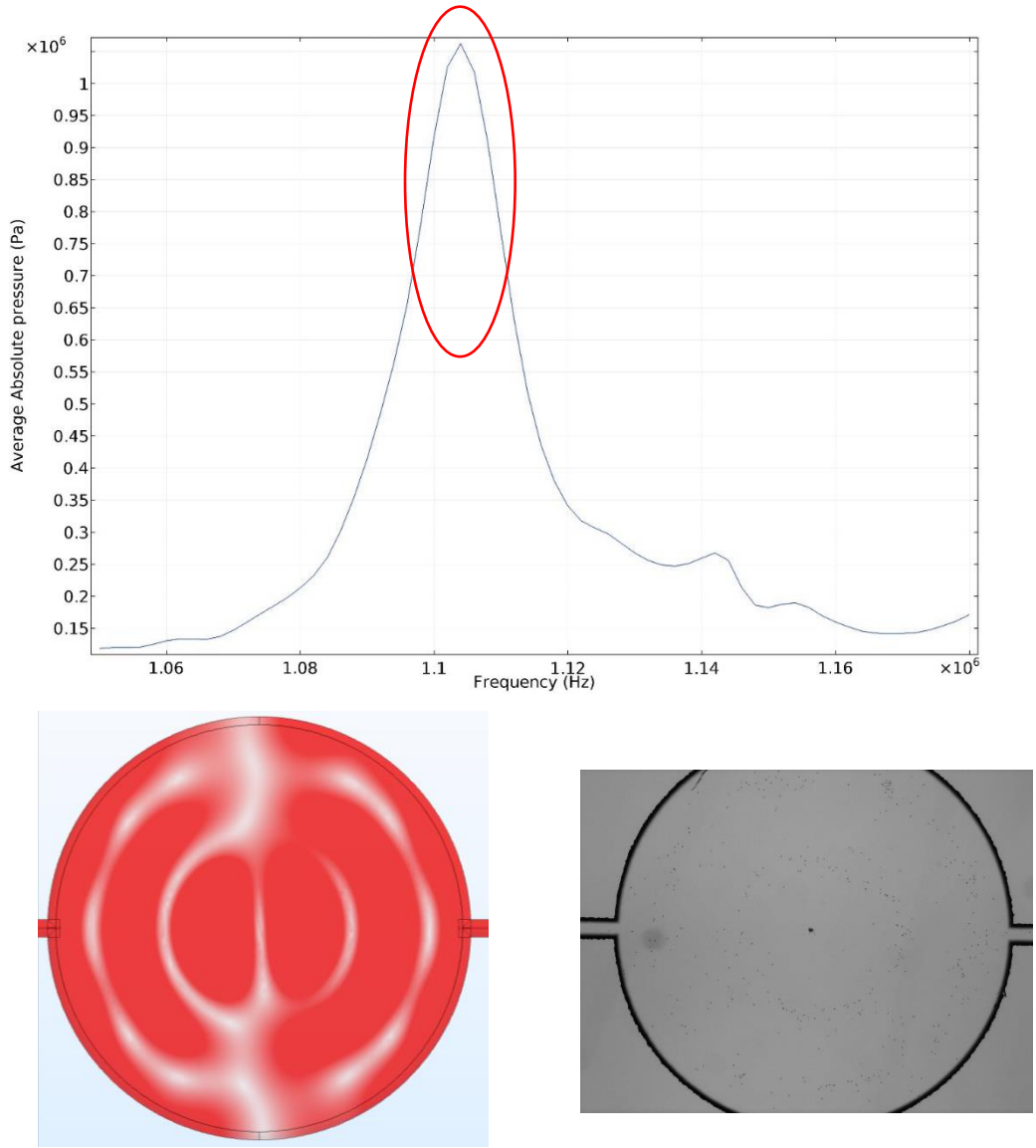

$1.104\ MHz$ $1.151\ MHz$

Figure 3.16 The frequency response of the 3D model for the circle channel case is shown at the top. The pressure map at the resonance frequency for the model is shown at the bottom left, compared to the experimental result at the bottom right.

3.4Discussion

For each geometric case, the resonance frequency and the absolute pressure field match very well with the experiments. Thus, the model building process achieves a satisfactory solution while balancing accuracy and computational expense as summarized below:

1. Properties of the piezoelectric material are tuned using experimental measurements by comparison of the predicted and experimental impedance responses. Improved accuracy may be achieved by tuning other material properties in the future; however, the piezoelectric properties have larger variability and are less well characterized than those of the glass and fluid.
2. A 2D cross-sectional model is built to efficiently locate resonant frequencies over a broad spectrum.
3. A 3D model is built and run over a narrower frequency range to find the exact resonance, which is verified using the map of the absolute pressure.

The 3D model has several features that ensure accurate results. Such features are listed below:

- The piezoelectric material is modeled fully since none of the dimensions are comparably much larger than the dimensions of other parts. The piezoelectric material is also the driving force of system vibration, and spatial effects influence the vibration mode. If the longitudinal direction is modeled the same way as the glass material by using the Low-Reflecting boundary condition and reduced size, the absolute pressure field will not be accurate.
- The borosilicate material and the etched fluid channel are modeled partially with the Low-Reflecting boundary condition and the Plane Wave Radiation boundary condition since the longitudinal dimension is much larger than the other assembly dimensions. The model is still accurate even though they are not modeled fully since spatial effects should be small, and the boundary conditions are set up to realistically capture the behavior of a full system.

In general, both models predict the resonant frequency of the devices very well, and the absolute pressure fields of the 3D model match well with the experiments.

4 Flagellum Model

4.1 Objectives: Investigation of Passive Structures and Flutter Instability

Many mechanisms are proposed to explain the oscillation of flagella. In this chapter, the theory, which states that steady dynein force together with fluid-structure interactions can induce the oscillation of flagella, is studied through the dynamic model. The static model with applied forces on flagella is used to study the passive structures of flagella by comparing the results with both theoretical and experimental works.

4.2 Procedure

4.2.1 Static Model: Investigation of Passive Structures

As mentioned in the introduction, a finite element model of a flagellum can be based on either a simplified 6-doublet model or a full 9-doublet model, where the 9-doublet model has additional degrees of freedom, and thus, is more computationally expensive for each nonlinear solution.

A 9-doublet model is used for the static study since a static model as computationally costly as a dynamic model. For a given static model, only one nonlinear solution is needed. However, the dynamic model involves time marching, necessitating a nonlinear solution at each time step.

The geometry setup is shown in Figure 4.1.

(a)

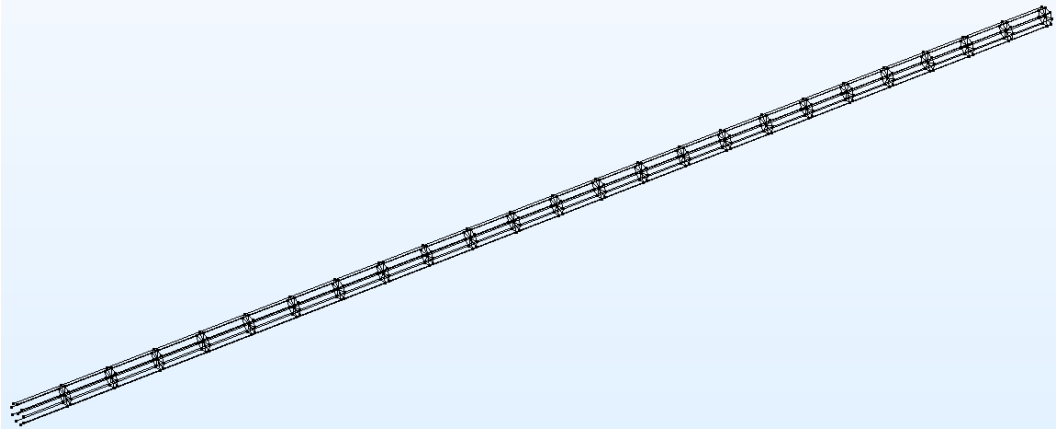

(b)

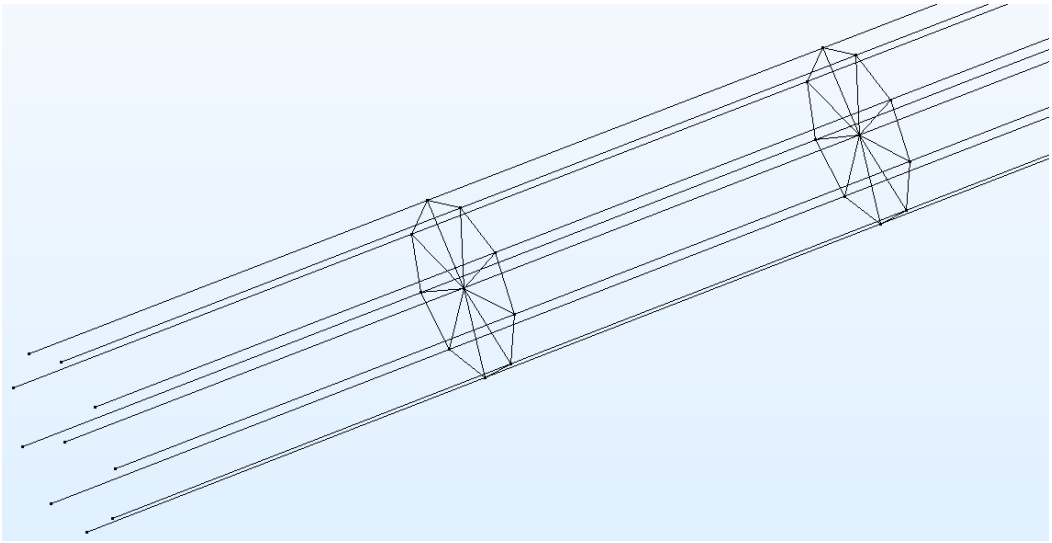

Figure 4.1 Geometry of the static model: (a) the general view (b) the zoomed-in view at the base.

The model consists of three types of passive structures as stated in the introduction. The doublets are shown as blue beams in Figure 4.2 (a); the radial spokes are shown as blue beams in Figure 4.2 (b); the nexin links are shown in Figure 4.2 (c). The material properties and dimensions are summarized in Table 4.1 and Table 4.2 respectively.

(a)

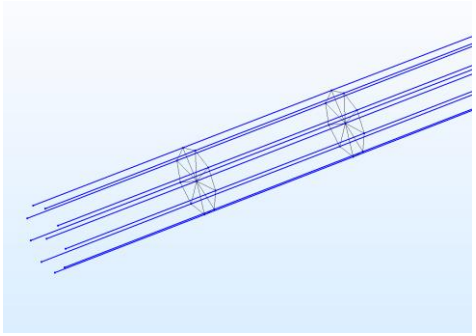

(b)

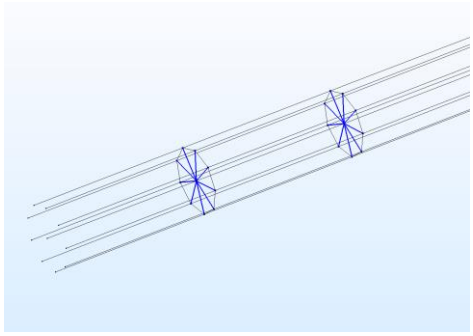

(c)

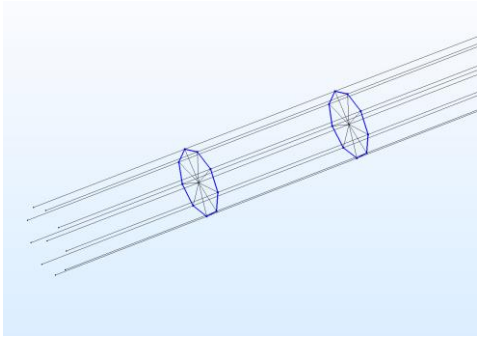

Figure 4.2 Beams represent (a) doublets, (b) radial spokes and (c) nexin links.

Table 4.1 The summary of all material properties.

Material Properties	Doublets	Radial Spokes	Nexin Links
Young's Modulus $[\boldsymbol{GPa}]$	$\mathbf{0.80}$	$\mathbf{25.46}$	$\mathbf{0.08}$
Poisson's Ratio $[\mathbf{1}]$	$\mathbf{0.40}$	$\mathbf{0.40}$	$\mathbf{0.40}$

Table 4.2 The summary of the dimensions for the static 9-doublet model.

Dimensions	Doublets	Radial Spokes	Nexin Links
Length $[\boldsymbol{nm}]$	$\mathbf{1.20 \times 10^4}$	$\mathbf{100.00}$	$\mathbf{68.40}$
Radius $[\boldsymbol{nm}]$	$\mathbf{20.00}$	$\mathbf{1.12}$	$\mathbf{1.12}$
Spacings between Each Section $[\boldsymbol{nm}]$	$\mathbf{500.00}$		

Only one physics, Beam Physics, is used for this model. The reasons that Beam Physics is used rather than Solid Mechanics are listed below:

- A model using Beam Physics has fewer degrees of freedom compared to a model using Solid Mechanics since the former is essentially a 1D model in 3D space. Fewer degrees of freedom ensure less computational time.
- For all components of the flagellum model, two of the three dimensions are much smaller than the third, which corresponds with the assumption of the Beam Physics, so solutions are still accurate even though a less hierarchical physics is used.

The Fix boundary condition is set for points as shown in Figure 4.3 (a). The mathematical form of the boundary condition is $\vec{u} = \vec{0}$ and $\vec{\theta} = \vec{0}$, where $\vec{u}$ and $\vec{\theta}$ are the displacement field and the rotational field, respectively, at the boundary point. This boundary condition ensures that the beam can neither move nor rotate at the fixed wall, and simulates that the base of the flagellum is fixed when connected to the cell body.

There are two cases studied using the finite element method. The first case is that the flagellum is loaded at the midpoint, and the other is that the flagellum is loaded at the endpoint. The boundary conditions of these two cases have the same mathematical form. $\vec{F} = \overrightarrow{F_p}$ and $\vec{M} = \overrightarrow{M_p}$, where $\vec{F}$ and $\vec{M}$ are the force and moment field respectively at the boundary point, and $\overrightarrow{F_p}$ and $\overrightarrow{M_p}$ are the given force and moment. Moments are set to be zero, but the forces are set to be $10\ \mathrm{pN}$ in the y direction for both cases. The endpoint case is shown in Figure 4.3 (b), and the midpoint case is shown in Figure 4.3 (c).

(a)

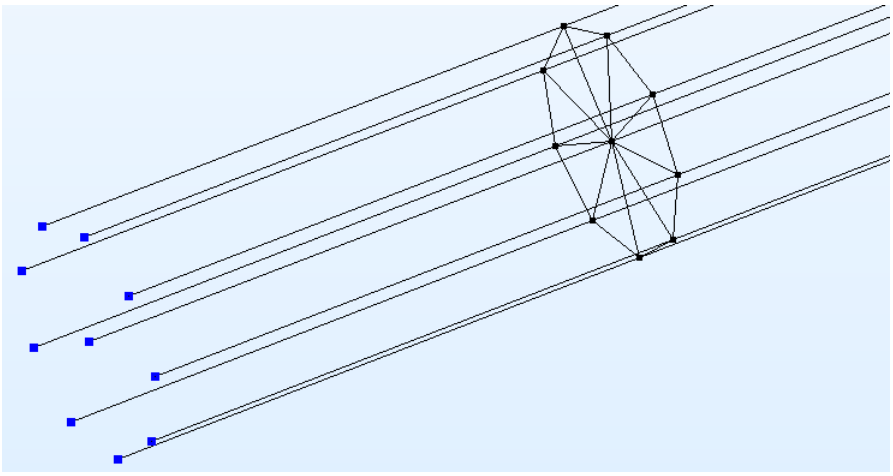

(b)

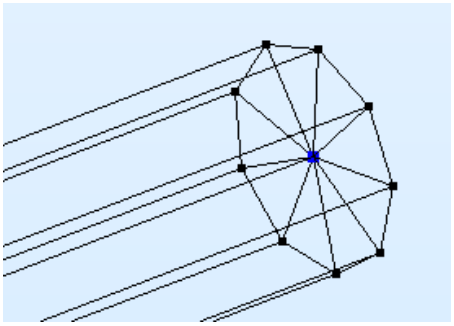

(c)

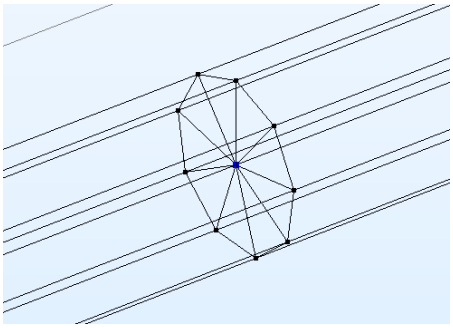

Figure 4.3 Boundary conditions: (a) Fixed, (b) Point Load for the case with midpoint load and (c) Point Load for the case with endpoint load

The mesh used for the model is summarized in Table 4.3. and the stationary solver is used to generate the results. Rotational field and displacement field are solved for the model and other results are extracted from these results. The maximum number of iterations is set to be 200 to make sure the nonlinear solver converges.

Table 4.3 Summary of the mesh setup for the static 9-doublet model.

	Doublets	Radial Spokes	Nexin Links
Mesh Element Size $[nm]$	**500.00**	**100.00**	**68.40**

4.2.2 Dynamic Model: Investigation of Flutter Instability

As stated in the previous section, the 6-doublet model is used for the dynamic model to reduce the computational time. The geometry is shown in Figure 4.4, with the details of a single segment also shown.

(a)

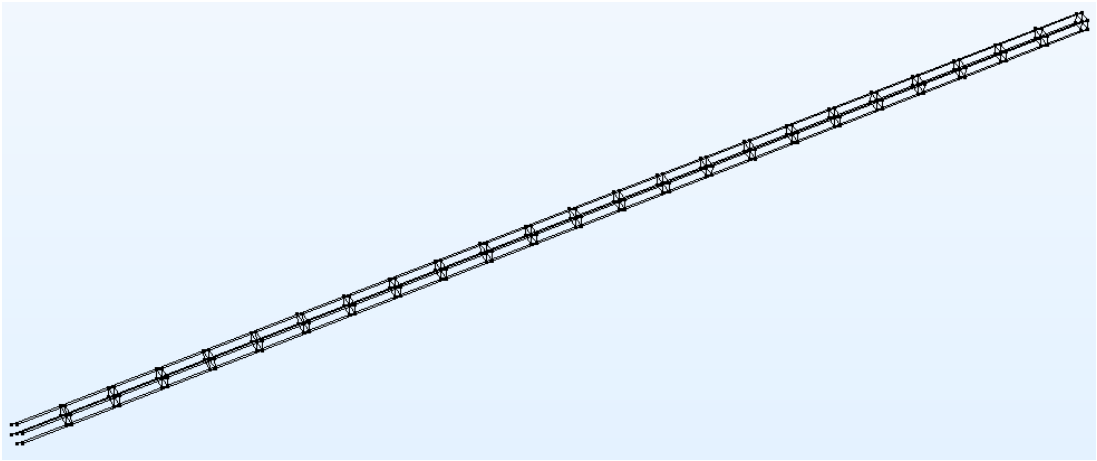

(b)

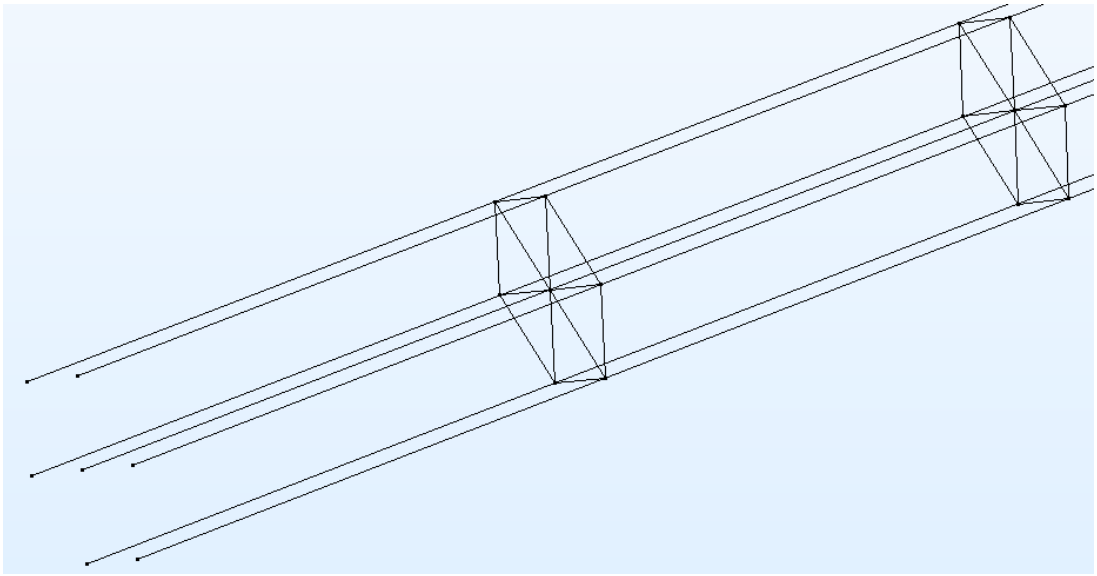

Figure 4.4 Geometry of the dynamic model: (a) the general view and (b) the zoomed-in at the base.

The setup of the three types of static structures is similar to the previous section. However, they are slightly different since there are only 6 doublets for this model. The doublets, radial spokes and nexin links are shown in Figure 4.5 (a), (b) and (c) respectively. The material properties are as listed in Table 4.1 **The summary of all material properties.**Table 4.1.

(a)

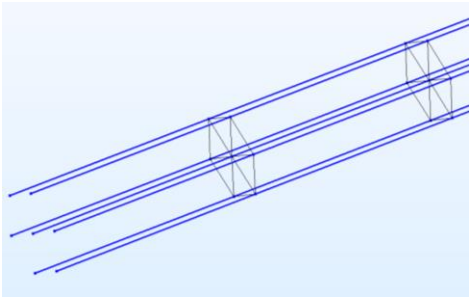

(b)

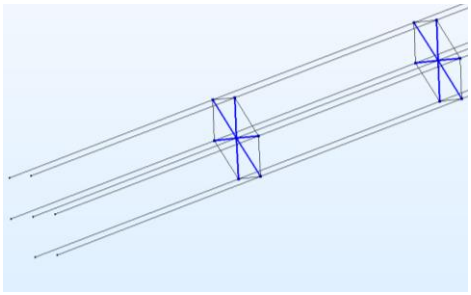

(c)

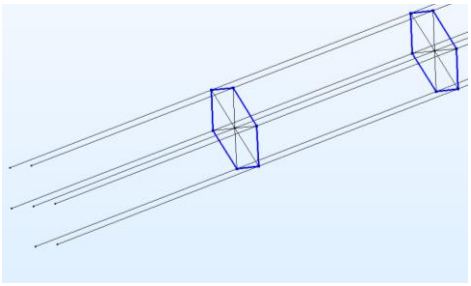

Figure 4.5 Beams represent (a) doublets, (b) radial spokes and (c) nexin links.

Again, only Beam Physics is used for the model. However, compared to the static model, this model has more complicated boundary conditions.

The Fix boundary conditions are set for the base points as shown in Figure 4.6 (a).

The Point Load boundary condition is set to the endpoint as shown in Figure 4.6 (b). This boundary condition is used to introduce imperfection into the system so that oscillation can be induced. The mathematical form for this boundary condition is $\vec{F} = \overrightarrow{F_p} = 0.3\vec{j}\,pN$ for $\mathrm{t} < 0.0001\mathrm{s}$, where $\vec{j}$ is the unit vector in the y direction. The point shown in the figure is subjected to a force with a magnitude of $0.3\ \mathrm{pN}$ and a direction of $(0,1,0)$ for the first $0.0001\mathrm{s}$.

The Edge Load boundary conditions are set for edges as shown in Figure 4.6 (c), (d) and (e) for tip-ward dynein force, base-ward dynein force, and the counter moment respectively. These boundary conditions simulate the effects of the dynein arms. The forces and the moments are added as distributed loads in the governing equation, and the local coordinate system is used rather than the global system, so the forces and the moments act as non-conservative follower forces which always have the same direction as the axial direction of the beams representing the doublets.

Another set of Edge Load boundary conditions is used for the edges as shown in Figure 4.6 (f), which are all the doublets. These boundary conditions are set to simulate the viscous resistance force due to the interaction between the flagellum and the fluid. The set of boundary conditions is only applied to the doublets since other structures are much smaller than the doublets, and the viscous effects can be neglected. The forces are applied as $\boldsymbol{F_{viscous}} = C_T\boldsymbol{u_{local}} + C_N\boldsymbol{v_{local}} + C_N\boldsymbol{w_{local}}$, where C_T is the tangential viscous coefficient and C_N is the normal one. $\boldsymbol{u_{local}}$, $\boldsymbol{v_{local}}$ and $\boldsymbol{w_{local}}$ are the local velocities, which can be calculated from the global velocities.

(a)

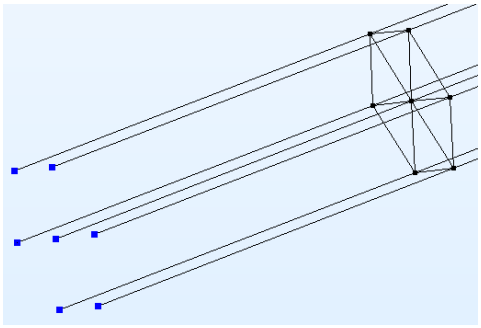

(b)

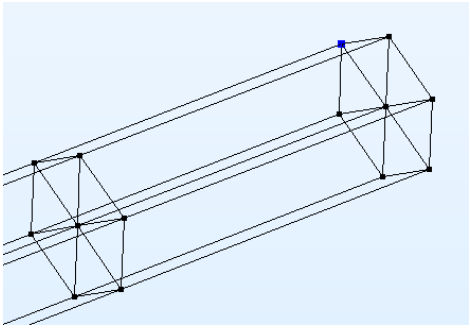

(c)

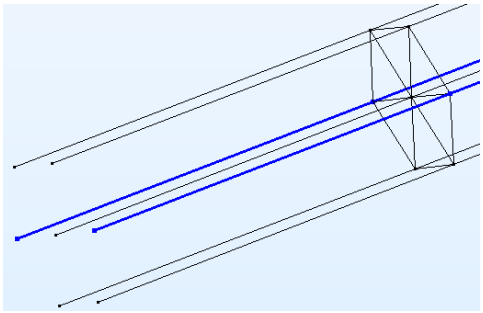

(d)

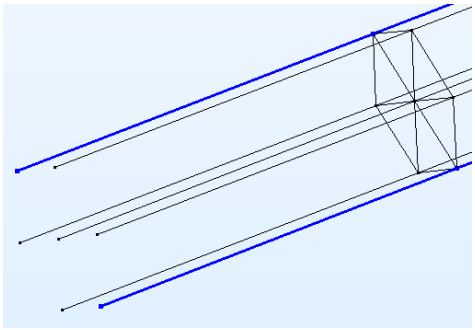

(e)

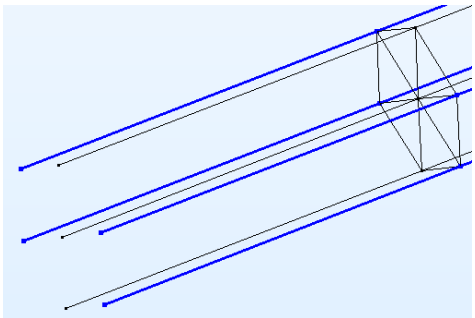

(f)

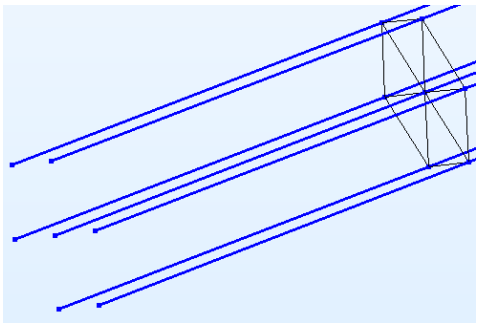

Figure 4.6 Boundary conditions: (a) Fixed, (b) Point Load, (c) Edge Load for the tip-ward dynein forces, (d) Edge Load for the base-ward dynein forces, (e) Edge Load for the counter moments and (f) Edge Load for the viscous resistance forces.

Three cases with increasing number of mesh elements are used for convergence study, and the setups are summarized in Table.

Table 4.4 Summary of the mesh setup for three cases with increasing number of mesh elements.

Mesh Element Size $[mm]$	Doublets	Radial Spokes	Nexin Links
Case **1**	**500.00**	**100.00**	**100.00**
Case **2**	**250.00**	**100.00**	**100.00**
Case **3**	**166.67**	**100.00**	**100.00**

4.3Results

4.3.1 Static Response to Applied Lateral Point Loads

The results of the static models with midpoint load and endpoint load are shown in Figure 4.7 and Figure 4.8 respectively. The displacement in the **y** direction is plotted on the deformed body and the magnitude is shown by color. Only the displacement in the **y** direction is shown because the forces are applied in the **y** direction. The counter bend is observed for the midpoint load case as expected from the theory as stated in the background theories.

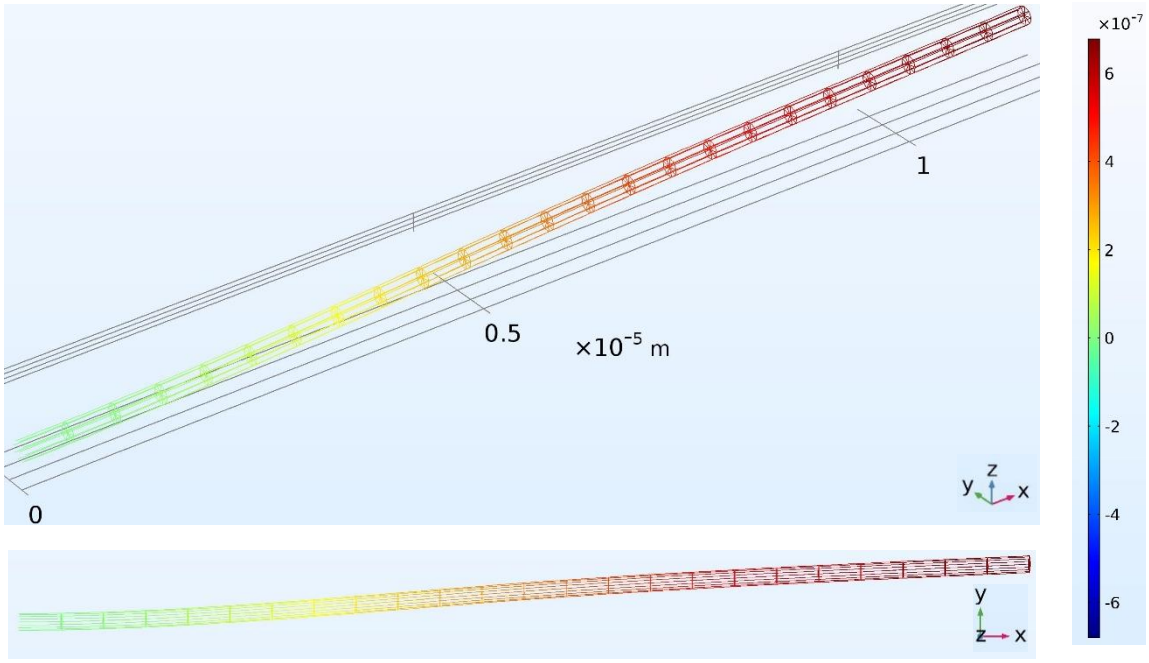

Figure 4.7 The magnitude of the displacement in y direction, shown by color, plotted on the deformed body with the general view at the top and the xy plane at the bottom. (Midpoint load)

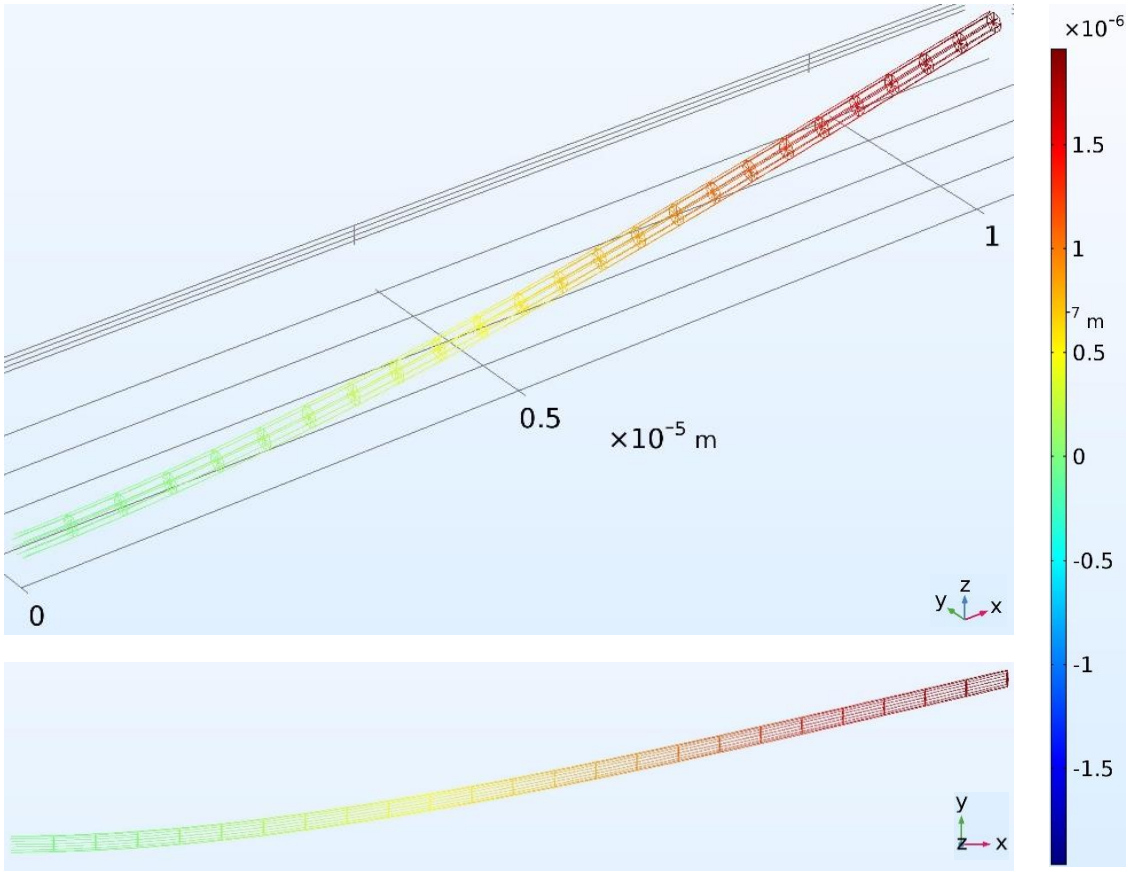

Figure 4.8 The magnitude of the displacement in $\boldsymbol{y}$ direction, shown by color, plotted on the deformed body with the general view at the top and the $\boldsymbol{xy}$ plane at the bottom. (Endpoint load)

4.3.2 Flutter Instability and Oscillatory Behavior

The results of the dynamic model for the given mesh are shown below. 3D view and 2D views in the yz planes and the xz planes for $t = 0.060$ s are shown in Figure 4.9. The color bar shows the magnitude of the axial stress within all beams. The oscillatory waveform is visually confirmed by checking animations of the plots from $t = 0.000$ s to $t = 0.060$ s.

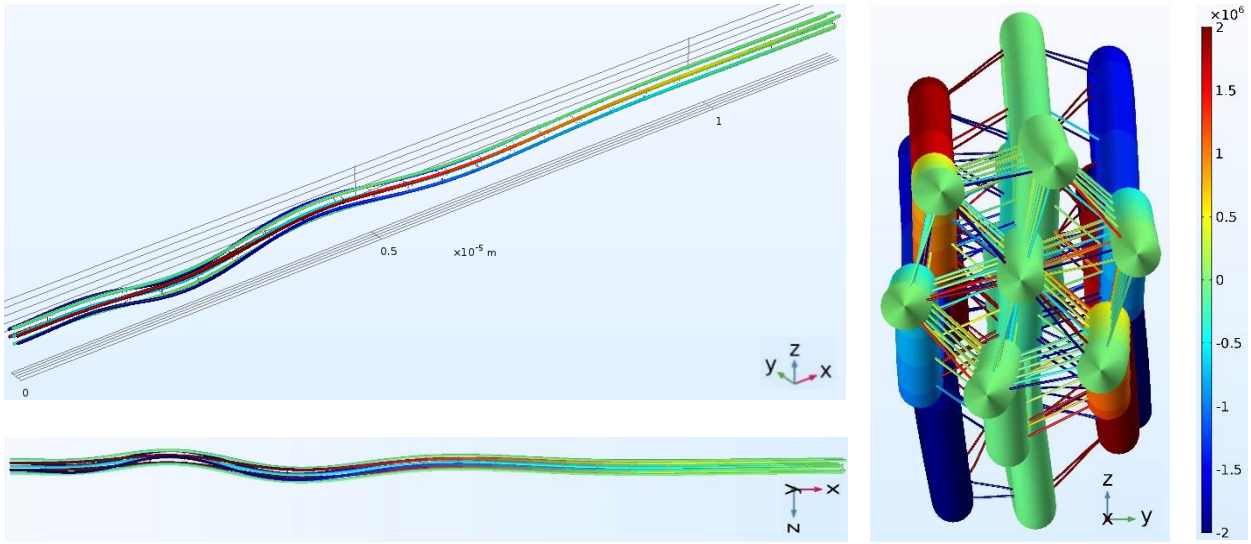

Figure 4.9 The magnitude of the axial stress, as shown by color, plotted on the deformed body for $t = 0.060\ s$ with the general view at the top left, the xz plane view at the bottom left and the yz plane at the right in tip-to-base direction.

Plots of midpoint displacement versus time in the z direction and in the y direction are shown in Figure 4.10 (a) and (b) respectively with the same scale. The magnitude of the displacement is much larger in the main oscillation direction than those in the perpendicular direction. Also, the oscillatory behavior is clearly seen in these plots.

(a)

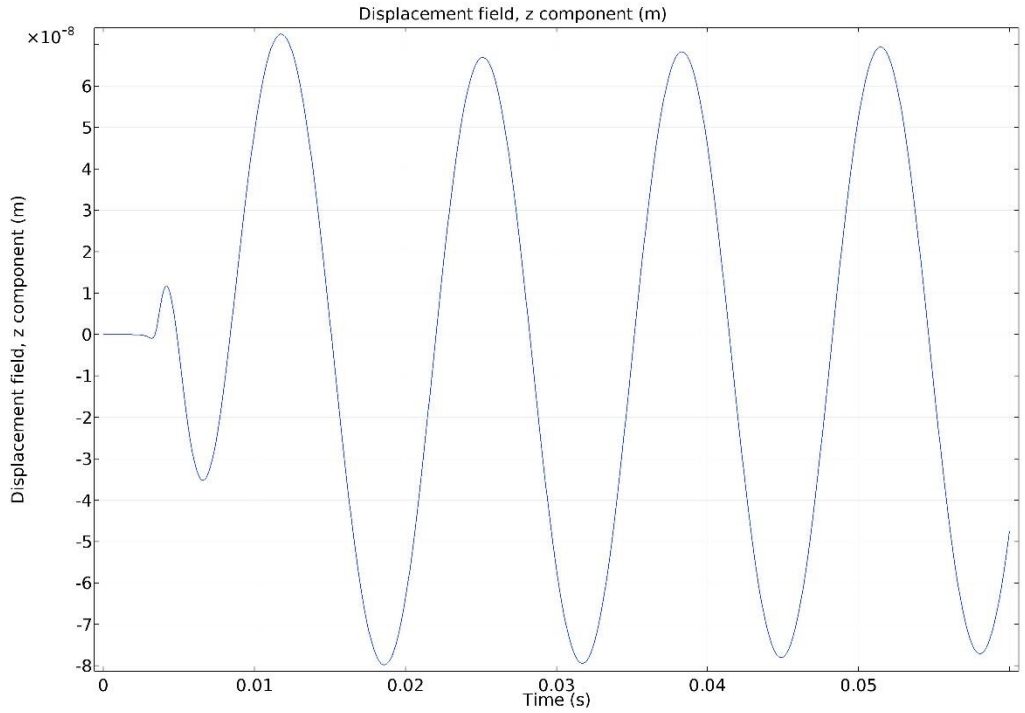

(b)

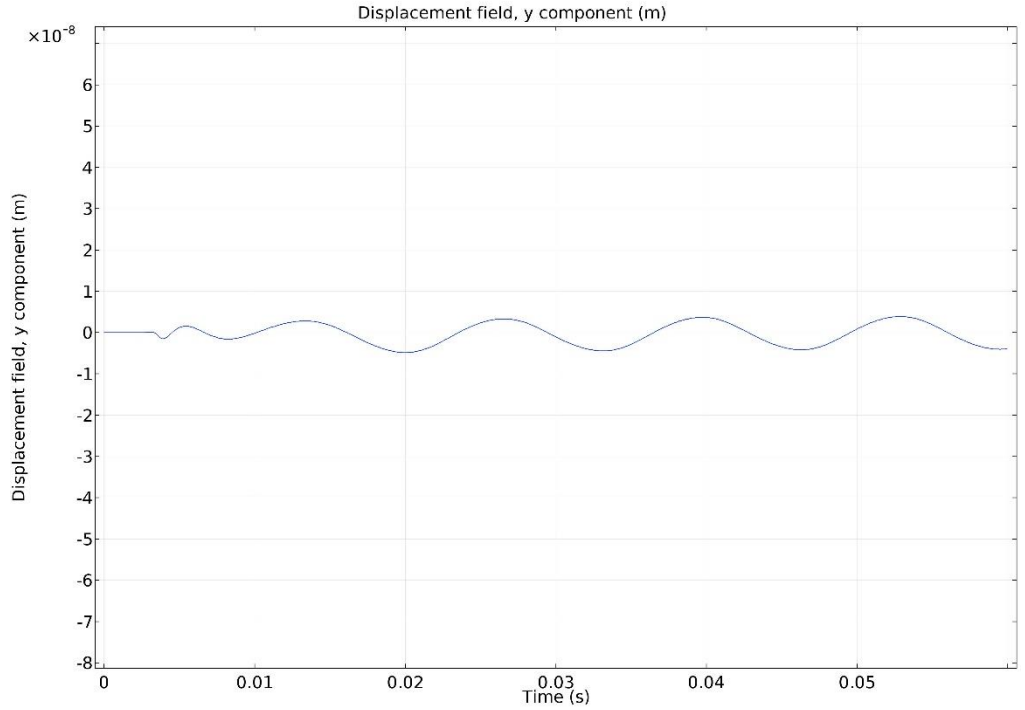

Figure 4.10 The magnitude of the displacement versus time for the dynamic model with the coarsest mesh (**456** elements) in (a) $\boldsymbol{z}$ direction and in (b) $\boldsymbol{y}$ direction.

As shown in both figures, the flagellum starts with no deformation and begins to oscillate after a transient process. The midpoint oscillation behavior is clear and steady through multiple periods and it indicates the oscillatory behavior of the whole flagellum. The period and the magnitude of the midpoint oscillation can be calculated by taking the average for these values over several periods. These values are global values characteristic of a given flagellum dynamic model. Thus, they can be used to check the convergence of the dynamic model. As discussed in the background theory, the mesh size can be used to control the degrees of freedom for a finite element method. For this dynamic model, three cases with increasing mesh elements are built for convergence study together, as stated in the previous section. Two plots of the magnitude and the period versus the number of degrees of freedom are shown in Figure 4.11 (a) and (b) respectively. Convergence behaviors are observed for both the frequency and the magnitude.

(a) (b)

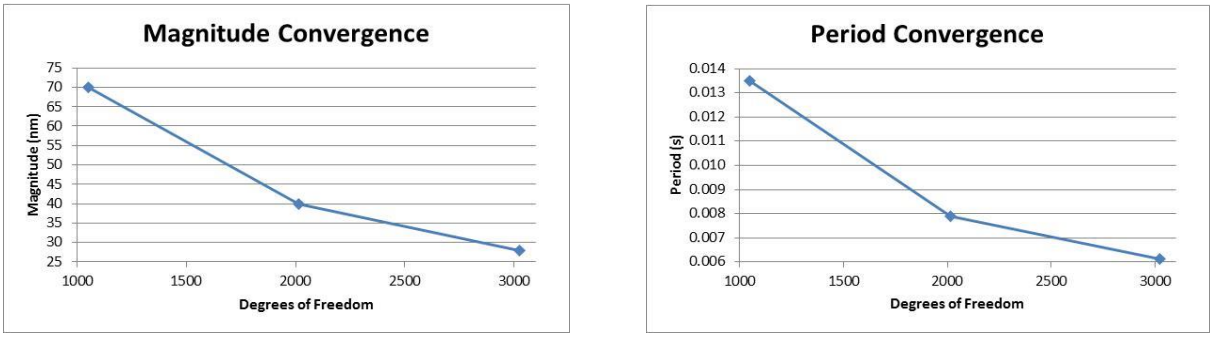

Figure 4.11 Convergence plot of (a) the maximum midpoint displacement in ***z*** direction and (b) the period of the oscillation.

4.4Discussion

For the static models, the bending shapes are as expected from the theory. If the model is one beam, the midpoint load will just cause it to bend without a counter bend. However, the counter bend is presented in the model since the model is a combination of beams. While the center doublet is being bent by the applied load, other doublets are resisting the bending by applying shear resistance forces onto the center doublet. Such shear resistance forces are applied through the nexin links and the radial spokes. Thus, the more complex model provides more insight into the operation of passive structures of flagella since experiments are limited due to the fact that flagella are very small in size.

Through the dynamic model, it is confirmed that steady dynein force together with structure-fluid interactions can initiate and maintain oscillation in flagella. The initiation process is made possible due to the disturbance force. However, such disturbance force is not necessary since imperfection is the nature of the materials and needs not to be introduced by a force.

5 Confinement of Swimming Cells in Acoustic Microfluidic Device

5.1 Objectives

There are mutual benefits to studying both acoustic microfluidic devices and swimming microorganisms in a single thesis. A well-characterized acoustic microfluidic device can be used to investigate the propulsive force generated by the waveform of *C. reinhardtii* cells by analyzing the spread of the swimming cells in the device. Similarly, the *C. reinhardtii* cells can be used as active probes for the pressure field in an acoustic microfluidic device.

This chapter introduces an ongoing effort to model the behavior of swimming cells confined within pressure wells of an acoustic microfluidic device. The proposed approach combines the two previous models through the balance between the acoustic radiation force and the swimming force. The acoustic radiation force can be calculated using the pressure field determined in Chapter 3, and the swimming force is related to the propulsive force extracted from the dynamic solution in Chapter 4.

5.2 Procedure

A particle tracing method is used rather than finite element method since only the behavior of swimming cells is of interest. In this model, a single cell of *C. reinhardtii* is treated as a spherical particle. The governing differential equation is $m\frac{\partial^2}{\partial t^2}\boldsymbol{u} = \boldsymbol{F}$, where $\boldsymbol{u}$ is the displacement of a particle, m is the mass of the particle and $\boldsymbol{F}$ is the total force experienced by the particle. $\boldsymbol{F} = \boldsymbol{F_{rad}} + \boldsymbol{F_{drag}} + \boldsymbol{F_{swimming}}$, where $\boldsymbol{F_{rad}}$ is the acoustic radiation force, $\boldsymbol{F_{drag}}$ is the drag force and $\boldsymbol{F_{swimming}}$ is the propulsive swimming force. The drag force is well-characterized as $\boldsymbol{F_{drag}} = 6\pi\mu a\boldsymbol{v}$, where μ is the viscosity of the fluid, a is the radius of the particle and $\boldsymbol{v}$ is the velocity of the particle. The relationship between the velocity and the displacement is shown in equation $\boldsymbol{v} = \frac{\boldsymbol{\partial}}{\boldsymbol{\partial t}}\boldsymbol{u}$. Thus, the governing equation can be now re-formulated as $m\frac{\partial^2}{\partial t^2}\boldsymbol{u} = 6\pi\mu a\frac{\partial}{\partial t}\boldsymbol{u} + \boldsymbol{F_{rad}} + \boldsymbol{F_{swimming}}$. If the properties and $\boldsymbol{F_{rad}} + \boldsymbol{F_{propulsive}}$ are known, the only dependent variable, the displacement $\boldsymbol{u}$, can be solved with proper boundary and initial conditions.

The acoustic radiation force can be calculated using Eqn. 2.13-2.15. Again, as stated in the background theory, the acoustic radiation force can be calculated if the properties and the pressure field are known. The pressure field is an output of the 3D model in Chapter 3. However, only a 2D pressure field generated at the central plane in the thickness direction of the 3D solution will be used for the following reasons:

- Tracking particles using the governing equation in 3D is more computationally expensive than in 2D.
- The thickness of the channel is the same order of magnitude of the size of the swimming cells, so movements of the cells in the thickness direction are limited.

If the 2D pressure field can be extracted from the 3D model, then the acoustic radiation force, $\boldsymbol{F_{rad}}$, will be a known in the governing equation.

The propulsive force is more complicated than the acoustic radiation force. It is observed from experiments that the *C. reinhardtii* swims almost straight with constant speed and reorients after a certain amount of time. It is natural to rewrite the propulsive force in terms of the direction and the magnitude of the force as $\boldsymbol{F_{propulsive}} = \boldsymbol{Dir}(t) \times Mag$, where $\boldsymbol{Dir}(t)$ is a unit vector indicating the swimming direction and Mag is the magnitude of the swimming force. $\boldsymbol{Dir}(t)$ is a function of time because the *C. reinhardtii* reorients after a certain time period has passed. However, Mag is not a function of time because *C. reinhardtii* swims almost with constant speed regardless the swimming direction.

The magnitude of the swimming force, Mag, can be calculated from the propulsive force generated by the two flagella. The base structural force of the flagellum model is the reaction force of the propulsive force based on Newton's Third Law, and it can be calculated from the displacement and rotation field, which are the solutions introduced in Chapter 4. The total swimming force is the sum of the propulsive forces generated by the two flagella. However, not only just one swimming cell will be modeled, but a group of cells. Even for cells with the same genetic background, the swimming forces are not the same. Here, the assumption is made that the magnitudes of the swimming forces for a group of cells form a normal Gaussian distribution with the mean value being the swimming force calculated from the dynamic model. When the particles representing the cells are initialized in the model, each of them will be given a specific Mag based on the normal distribution.

For the direction vector, $\boldsymbol{Dir}(t)$, it is assumed that the cells can reorient to any angle with no limit. The reorientation time for a group of cells is assumed to be a normal Gaussian distribution for the same reason as stated above. The average reorientation time and the standard deviation, however, are unknown for now, but they can be obtained from a statistical study of the experimental results. Example plots of reorientation angle versus time are shown in Figure 5.1. Whenever a cell reorients, the reorientation angle is random, but the reorientation time fits a normal Gaussian distribution with set mean and standard deviation, which can be changed as shown in Figure 5.1.

(a)

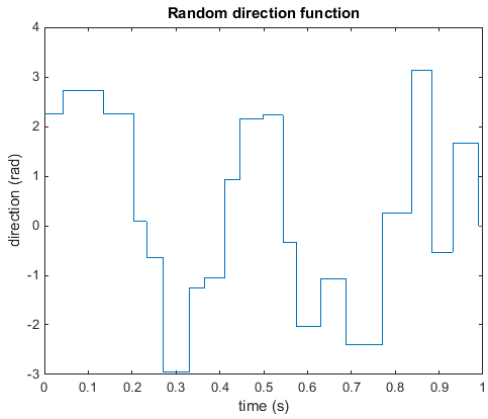

$Mean = 0.05\ s$ and $STD = {}^{0.05}/_{3}\ s$

(b)

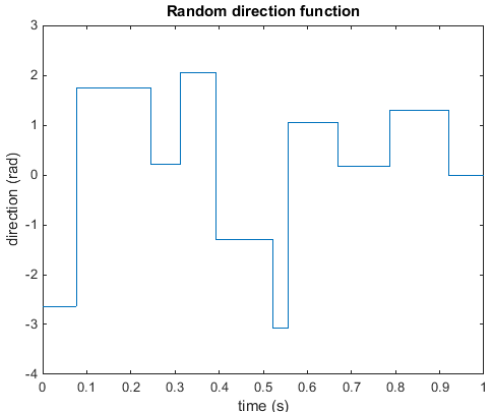

$Mean = 0.10\ s$ and $STD = {}^{0.10}/_{3}\ s$

(c)

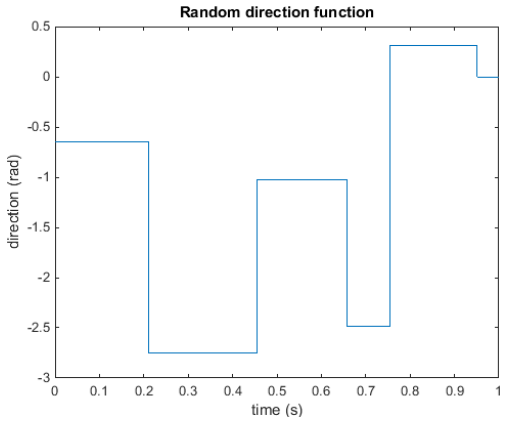

$Mean = 0.20\ s$ and $STD = {}^{0.20}/_{3}\ s$

(d)

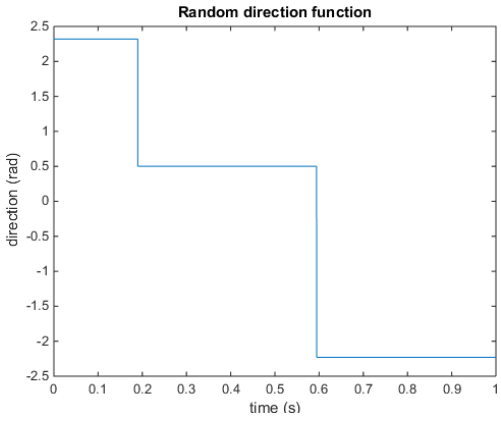

$Mean = 0.40\ s$ and $STD = {}^{0.40}/_{3}\ s$

Figure 5.1 Reorientation angles versus time for various mean values and standard deviations.

The displacement of each particle can be solved now as it is the only unknown variable in the governing equation with initial conditions including position, velocity, Mag and $\boldsymbol{Dir}(t)$ given to the particles.

Conclusion

The general goal of this thesis is to use simulation and modeling to study *C. reinhardtii* from micro-scale to nano-scale. The finite element models of the acoustic microfluidic devices indicate that the devices generate patterns of pressure wells suitable for trapping groups of cells. Such devices are very useful for confinement and investigation of rapidly swimming cells and microorganisms including *C. reinhardtii*. The results of the models correspond with those of the experiments. The static nano-scale model will be used for the structural study of flagella. The dynamic nano-scale model computationally and theoretically confirms that steady dynein forces together with structure-fluid interaction can induce oscillatory waveform of flagella. Further study of the waveform can be done through the same model by changing the viscous resistance coefficients, material properties, etc. Also, these models serve as building blocks of the particle tracing model, where the pressure fields and the propulsive forces are used as inputs. The particle tracing model will enable complementary studies of both acoustic microfluidic devices and the *C. reinhardtii* as discussed in the introduction and in Chapter 5.

Future research work will focus on refinement of the nano-scale flagellum model and the particle tracing model. Additional modifications for current models will include:

- Hierarchical models of the acoustic microfluidic devices with full dimensions to check the accuracy of the current simplified 3D model.
- A mesh stability study for the static nano-scale flagellum model.
- A hierarchical 9-doublet model for the dynamic nano-scale model to validate the current 6-doublet model.

Reference

[1] I. Gibbons, "Cilia and flagella of eukaryotes," *Journal of Cell Biology,* vol. 91, no. 3, 1981.

[2] P. Bayly and S. Dutcher, "Steady dynein forces induce flutter instability and propagating waves in mathematical models of flagella," *J. R. Soc. Interface,* vol. 13, no. 20160523, 2016.

[3] G. Pazour, N. Agrin, B. Walker and G. Witman, "Identification of predicted human outer dynein arm genes: candidates for primary ciliary dyskinesia genes," *Journal of Medical Genetics,* vol. 43, no. 1, 2006.

[4] M. Fliegauf, T. Benzing and H. Omran, "Mechanisms of disease - When cilia go bad: cilia defects and ciliopathies," *Nature Reviews Molecular Cell Biology,* vol. 8, no. 11, 2007.

[5] W. Marshall, "The cell biological basis of ciliary disease," *Journal of Cell Biology,* vol. 180, no. 1, pp. 17-21, 2008.

[6] C. Silflow and P. Lefebvre, "Assembly and motility of eukaryotic cilia and flagella: Lessons from Chlamydomonas reinhardtii," *Plant Physiology,* vol. 127, no. 4, 2001.

[7] Z. L. El, H. Omran and P. Bouvagnet, "Lateralization defects and ciliary dyskinesia: lessons from algae," *Trends in Genetics,* vol. 19, no. 3, 2003.

[8] L. Keller, E. Romijn, I. Zamora, J. Yates and W. Marshall, "Proteomic analysis of isolated Chlamydomonas centrioles reveals orthologs of ciliary-disease genes," *Current Biology,* vol. 19, no. 3, 2005.

[9] J. Guasto, K. Johnson and J. Gollub, "Oscillatory Flows Induced by Microorganisms Swimming in Two Dimensions," *Physical Review Letters,* vol. 105, no. 16, 2010.

[10] H. Kurtuldu, D. Tam, A. Hosoi, K. Johnson and G. JP, "Flagellar waveform dynamics of freely swimming algal cells," *Physical Review E,* vol. 88, no. 1, 2013.

[11] B. Qin, A. Gopinath, J. Yang, J. Gollub and P. Arratia, "Flagellar Kinematics and Swimming of Algal Cells in Viscoelastic Fluids," *Scientific Reports,* vol. 5, no. 7, 2015.

[12] W. Coakley, D. Bardsley, M. Grundy, F. Zamani and D. Clarke, "CELL MANIPULATION IN ULTRASONIC STANDING WAVE FIELDS," *Journal of Chemical Technology and Biotechnology,* vol. 44, no. 1, 1989.

[13] S. Hagsater, T. Jensen, H. Bruus and J. Kutter, "Acoustic resonances in microfluidic chips: full-image micro-PIV experiments and numerical simulations," *Lab on a Chip,* vol. 67, no. 70, 2007.

[14] H. Bruus, "Acoustofluidics 7: The acoustic radiation force on small particles," *Lab on a Chip,* vol. 12, no. 6, 2012.

[15] P. Glynne-Jones, P. Mishra, R. Boltryk and M. Hill, "Efficient finite element modeling of radiation forces on elastic particles of arbitrary size and geometry," *Journal of the Acoustical Society of America,* vol. 133, no. 4, 2013.

[16] T. Lilliehorn, U. Simu, M. Nilsson, M. Almqvist, T. Stepinski, T. Laurell, J. Nilsson and S. Johansson, "Trapping of microparticles in the near field of an ultrasonic transducer," *Ultrasonics,* vol. 43, no. 5, 2005.

[17] A. Neild, S. Oberti, G. Radziwill and J. Dual, "Simultaneous positioning of cells into two-dimensional arrays using ultrasound," *Biotechnology and Bioengineering,* vol. 97, no. 5, 2007.

[18] S. Oberti, A. Neild and J. Dual, "Manipulation of micrometer sized particles within a micromachined fluidic device to form two-dimensional patterns using ultrasound," *ournal of the Acoustical Society of America,* vol. 121, no. 2, 2007.

[19] J. Svennebring, O. Manneberg, P. Skafte-Pedersen, H. Bruus and M. Wiklund, "Selective Bioparticle Retention and Characterization in a Chip-Integrated Confocal Ultrasonic Cavity," *Biotechnology and Bioengineering,* vol. 103, no. 2, 2009.

[20] O. Manneberg, B. Vanherberghen, J. Svennebring, H. Hertz, B. Onfelt and W. M, "A three-dimensional ultrasonic cage for characterization of individual cells," *Applied Physics Letters,* vol. 93, no. 6, 2008.

[21] B. Szabó and I. Babuška, Introduction to Finite Element Analysis: Formulation, Verification and Validation, Chichester, UK: John Wiley & Sons, Ltd., 2011.

[22] J. Dual and D. Moller, "Acoustofluidics 4: Piezoelectricity and Application in the Excitation of Acoustic Fields for Ultrasonic Particle Manipulation," *Lab on a Chip,* vol. 12, no. 3, 2012.

[23] P. M. Morse and K. U. Ingard, Theoretical Acoustics, Princeton University Press, 1986.

[24] L. E. Kinsler, A. R. Frey, A. B. Coppens and J. V. Sanders, Fundamentals of Acoustics, Wiley, 2000.

[25] H. Bruus, "Acoustofluidics 2: Perturbation Theory and Ultrasound Resonance Modes," *Lab on a Chip,* vol. 12, no. 1, 2012.

[26] "COMSOL Multiphysics Reference Manual, version 5.3," COMSOL, Inc., 2017.

[27] K. Yosioka and Y. Kawasima, "Acoustic Radiation Pressure on a Compressible Sphere," *Acta Acust. united with Acust.,* vol. 5, no. 3, 1955.

[28] L. P. Gor'kov, "'On the Forces Acting on a Small Particle Placed in an Acoustical Field of an Ideal Liquid," *Sov. Phys. Dokl,* vol. 6, no. 9, 1962.

[29] C. Brokaw, "Bend propagation by a sliding filament model for flagella," *Journal of Experimental Biology,* vol. 55, pp. 289-304, 1971.

[30] M. Murase, M. Hines and J. Blum, "Properties of an excitable dynein model for bend propagation in cilia and flagella," *Journal of Theoretical Biology,* vol. 139, pp. 414-430, 1989.

[31] C. Lindemann, "A model of flagellar and ciliary functioning which uses the forces transverse to the axoneme as the regulator of dynein activation," *Cell Motil. Cytoskeleton,* vol. 29, pp. 141-154, 1994.

[32] T. Hu and P. Bayly, "Finite element models of flagella with sliding radial spokes and interdoublet links exhibit propagating waves under steady dynein loading," *Cytoskeleton,* vol. 00, pp. 1-15, 2018.

[33] R. W. Clough, "Original formulation of the finite element method," *Finite Elem. Anal. Des.,* vol. 7, no. 2, pp. 89-101, 1990.

[34] O. C. Zienkiewicz and Y. K. Cheung, Finite Element Method in Structural and Continuum Mechanics: Numerical Simulation of Problems in Structural and Continuum Mechanics, U.K.: McGraw-Hill, 1967.

[35] B. Ivo and A. K. Aziz, Lectures on the Mathematical Foundations of the Finite Element Method, University of Maryland, 1972.

[36] I. Babuška and T. Strouboulis, The Finite Element Method and Its Reliability, Clarendon Press, 2001.

[37] K. J. Bathe, Finite Element Procedures, Prentice Hall, 2006.

[38] A. I. Ltd., "Material Properties of Lead Zirconate Titanate (PZT-8) Material 880," [Online]. Available: www.americanpiezo.com. [Accessed 30 4 2018].

[39] L. A. International, "Physical and Piezoelectric Properties of APC Materials," 2017. [Online]. Available: https://www.americanpiezo.com/apc-materials/piezoelectric-properties.html. [Accessed 30 4 2018].